Chapter 4 Multiscale Dynamics of the Tonga-Kermadec Subduction Zone

Abstract

Our understanding of mantle convection and the motion of plates depends on the viscosity structure of the mantle. While geoid and gravity observations have provided fundamental constraints on the radial viscosity structure of the mantle, the influence of short wavelength variations in viscosity is still poorly understood. Individual observations are not capable of constraining the 3-D viscosity structure within the subduction zone due to tradeoffs that render some observations insensitive to certain variations in viscosity or buoyancy. We present 2-D and 3-D finite element models of Stokes flow including strong lateral viscosity variations and local sources of buoyancy due to both thermal and compositional effects. We first use generic 2-D models of a subduction zone to investigate how different observations depend on various aspects of the viscosity structure, in particular, the slab and lower mantle viscosity and the presence of a low viscosity region in the wedge. We find that (1) strain-rate provides a strong constraint on the absolute viscosity of the slab, (2) stress orientation within the slab is sensitive to the relative viscosity of the slab, lower mantle and the wedge, and (3) the stress state and topography of the overriding plate depend on the wedge viscosity and local sources of buoyancy. We then use observations of strain-rate, stress orientation, dynamic topography and the geoid for the Tonga-Kermadec subduction zone as simultaneous constraints on the viscosity and buoyancy in a 3-D regional dynamic model. Together these observations are used to develop a self-consistent model of the viscosity and buoyancy by taking advantage of the sensitivity of each observation to different aspects of the dynamics over a broad range of length-scales. The presence of a low viscosity wedge makes it possible to match observations of shallow dynamic topography and horizontal extension over the back arc region and down-dip compression in the shallow portion of the slab. These results suggest that a low viscosity wedge may play an important role in controlling the presence of back arc spreading. However, for a model with a low viscosity and low density region which provides a good fit to the observed topography, we find that a reduction of

the slab density by a factor of two is required to match the observed geoid. These results suggests that compensation of the slab by dynamic topography may be a much smaller effect at short to intermediate wavelengths than predicted by long wavelength modeling of the geoid.

4.1 Introduction

The multiscale nature of dynamics within the earth is easily seen in the observed geoid (Figure 4.1) and bathymetry (Figure 4.2) in the region surrounding the Tonga-Kermadec subduction zone. The observed geoid is dominated by a very long wavelength (> 5000 km) increase in geoid height by 100 m from south to north and 40 m from east to west. Superimposed on this long wavelength signal the Tonga-Kermadec and New Hebrides Trenches are marked by small 10 m, short wavelength ($\sim$100 km) geoid lows. The observed bathymetry is dominated by short to intermediate (500–1000 km) wavelength signal due to variations in crustal thickness including the continental fragments making up New Zealand, the Chatham Rise, Campbell Plateau and Lord Howe Rise and lithospheric age including very young back arc spreading centers above the Tonga-Kermadec and New Hebrides subduction zones (Lau Basin, Havre Trough and Fiji Basins). At shorter wavelengths, the location of remnant and active island arcs (the Coleville and Tonga-Tofua Ridges) are apparent as are the trenches marking the subduction zones; these are the largest signals observed in the bathymetry with depths exceeding 4–5 km relative to abyssal depths. Recently (0–5 Ma) very fast subduction ($\sim$20 cm/yr total convergence) has been accompanied by active back arc spreading and slab rollback along the Tonga-Kermadec subduction zone. This style of subduction has been present in the region for at least 45 Ma creating a series of remnant arcs and extensional basins from the eastern edge of the Lord Howe Rise to the present-day active margin [Kroenke, 1984].

While the full spectrum of the dynamic response of the earth displayed in these observations reflects the scale of variation in the mantle, in terms of both driving forces and viscosity structure, studies of the dynamics have independently focused on the behavior at the very longest wavelengths (> 5000 km) or the very shortest (100–500 km) wavelengths. Here we begin to merge the understanding we have gained from these previous studies using finite element models of Stokes flow including strong variations in viscosity, local sources of buoyancy and a fault interface along plate boundaries to study the multiscale dynamics in a subduction zone. Our study is motivated by the increasing number of indirect observations (seismic, geochemical,

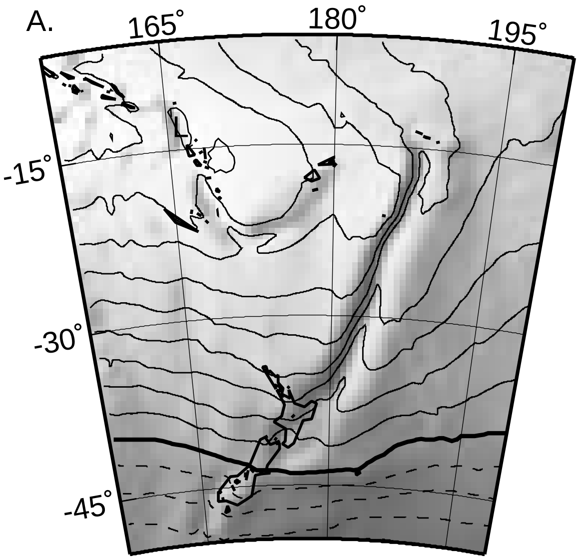

Figure 4.1: Observed geoid [Lemoine et al., 1998] for harmonic degrees L = 2–360 for the region of the Tonga-Kermadec subduction zone. Contour interval is 10 m, (dashed, negative; solid, positive; thick-solid, zero). Gray image highlights smaller scale relief on the longer wavelength geoid.

rock mechanics) that indicate that local, lateral variations in viscosity may play an important role in the dynamics of subduction zones and mantle convection.

4.2 Dynamic Modeling Constraints on Viscosity

4.2.1 Long Wavelength Geoid and Topography

Global modeling of the very long wavelength geoid has illustrated the importance of the dynamic response of the mantle, demonstrating the compensation of density anomalies within the mantle by flow-induced deformation of the surface and core-mantle boundaries and placing strong constraints on the radial structure of viscosity in the mantle. Several studies [Richards and Hager, 1984; Hager, 1984; Ricard et al., 1988; Vigny et al., 1991; Thoraval and Richards, 1997; Wen and Anderson, 1997] have shown that the very long wavelength geoid (harmonic degrees L = 2–9) can be explained by a radially stratified viscosity structure. While the details of these studies vary, the main conclusions are: (1) there is a jump in viscosity by a factor of 30–100 from the upper to the lower mantle [Richards and Hager, 1984; Hager, 1984; Hager et al., 1985; Hager and Clayton, 1989; Hager and Richards, 1989], (2) the L = 2–3 variation of the geoid is due to lower mantle density anomalies [Hager et al., 1985; Hager and Clayton, 1989; Hager and Richards, 1989] and (3) the L = 4–9 variation of the geoid, correlated with the locations of slabs in the upper mantle, is best fit by a viscosity structure with a weak lithosphere [Hager, 1984; Hager and Clayton, 1989].

As discussed by Richards and Hager [1984] and Hager [1984], the key to inferring the viscosity structure for a dynamic Earth from the geoid is that the observed geoid is the small difference between two large contributions of opposite sign: the contribution from internal density anomalies due to thermal or mineralogical variations and the contribution from the flow induced deformation of the boundaries (dynamic topography). While these studies predict up to several kilometers of long wavelength dynamic topography at the surface, it is difficult to assess whether these predictions match observations, because near-surface density variations at shorter wavelengths, including subduction zones, mask this signal. This creates a fundamental ambiguity in constraining viscosity with only observations of the geoid: while the wavelength dependence of the geoid gives some sensitivity to the depth and amplitude of density anomalies, a trade-off remains between the size and location of density anomalies and the viscosity structure (due to the dynamic topography on boundaries). Seismic tomography can be used to constrain the location of density anomalies [Hager and Clayton, 1989]. However, the relationship between seismic velocity anomalies and density is not well known [Dziewonski and Anderson, 1981].

The models discussed above suggest that density anomalies within the mantle are due to temperature variations, but ignore the strong temperature dependence of viscosity by including only radial variations in viscosity. This assumption makes an analytic solution to the flow possible, and later studies have argued that small variations in viscosity (less than 10×) expected in the lower mantle would have little effect on the very long wavelength geoid predicted by radially stratified models [Richards and Hager, 1989]. However, larger variations in viscosity associated with slabs, continents or weak plate boundaries in the upper mantle may influence the results at shorter wavelengths ($L > 4$) [Ravine and Morgan, 1993; Zhang and Christensen, 1993]. An example of the possible influence of lateral variations on the inferred radial structure is that the geoid correlated with slabs is better fit by a radial viscosity structure with a weak lithosphere rather than a strong lithosphere and that this difference in the inferred viscosity structure may be due to locally weak plate boundaries above slabs [Hager, 1984]. In addition, Koch and Ribe [1989] suggested that ignoring the strength of the slabs underestimated surface deformation and therefore would lead to an underestimate of the jump in the viscosity from the upper to the lower mantle.

Numerical models of viscous flow have been used to investigate the influence of large (10–1×10^4) lateral variations in viscosity [Sabadini et al., 1992; Zhong and Davies, 1999; Moresi and Gurnis, 1996]. In a 3-D model of the Mariana subduction zone, Moresi and Gurnis [1996] found that a jump in viscosity, from the upper to the lower mantle , larger than predicted by radial models, was needed if a slab in contact with the lower mantle was stronger than the surrounding asthenosphere. However, they were not able to match the observed short wavelength geoid or the long or short wavelength dynamic topography. This result demonstrates a disturbing reality of inferring a multiscale viscosity structure from the geoid: the very long wavelength geoid is not very sensitive to lateral variations in viscosity and a reasonable fit to the geoid is possible even when the dynamic topography does not agree with observations. This suggests that it is necessary to use multiple observations as simultaneous constraints on the 3-D viscosity structure.

4.2.2 Short Wavelength Topography and Gravity

Modeling of topography in subduction zones has traditionally focused on the flexural response of the lithosphere as either an elastic, viscous or elasto-plastic plate subject to a force or displacement near the trench [Bodine and Watts, 1979; Turcotte et al., 1978; Melosh, 1978]. These models successfully recreate the morphology of the trench including the forebulge. However, since the influence of the slab buoyancy force and flow in the mantle are not included, this approach can not be used to infer the viscosity structure or driving forces responsible for forming the trench. Kinematic and dynamic numerical models of viscous flow have been used to investigate the causes of short wavelength topography and gravity in subduction zones [McAdoo, 1982; Sleep, 1975]. Sleep [1975] attempted to model the topography and gravity for

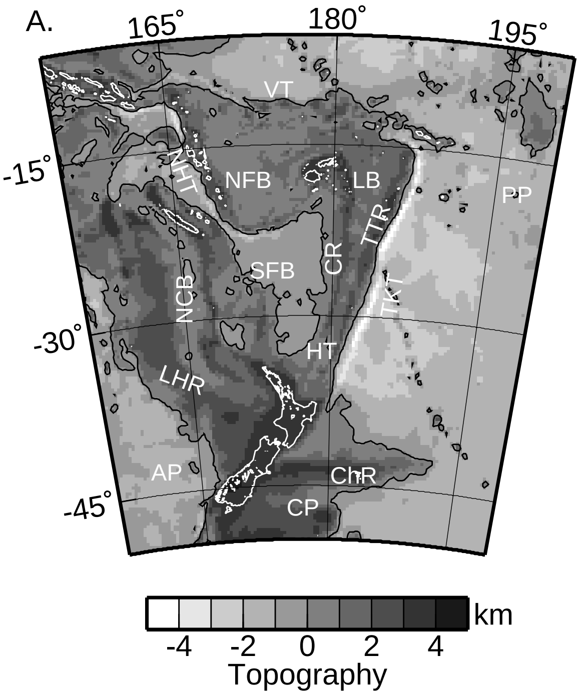

Figure 4.2: Observed Bathymetry [GEBCO, 1997] for the region of the Tonga-Kermadec subduction zone. Depths are shifted up by 3.5 km for comparison with model results. This places the abyssal depths of the Pacific Plate at ~0 km depth (marked by the black contour). TKT, Tonga-Kermadec Trench; NHT, New Hebrides Trench; VT, Vitiaz Trench; CR, Coleville Ridge; TTR, Tonga-Tofua Ridge; LB, Lau Basin; HT, Havre Trough; NFB, N. Fiji Basin; SFB, S. Fiji Basin; ChR, Chatham Rise; CP, Campbell Plateua; LHR, Lord Howe Rise; NCB, New Caledonia Basin; PP, Pacific Plate; AP, Australian Plate.

the Aleutian subduction zone using numerical models of 2-D Newtonian viscous flow. These models included crustal thickness variations based on seismic observations, the slab buoyancy based on the location of seismicity, temperature dependent viscosity and weak zones along the plate boundary and beneath the island arc. A match to both the gravity and topography was not found in part because the plate boundary was modeled as a weak zone without a fault and needed a very dense slab to match the trench depth.

Dynamic models of subduction zones that include a fault along the plate boundary have successfully reproduced trench morphology [Zhong and Gurnis, 1994; Zhong et al., 1998; Zhong and Gurnis, 1992; Buiter et al., submitted] and the long wavelength geoid [Zhong and Gurnis, 1992]. These models include radial and temperature dependent Newtonian or non-Newtonian viscosity, density anomalies due to the thermal anomaly of the slab and in some cases crustal thickness variations on the overriding plate [Zhong and Gurnis, 1994]. However, contrary to observations, these models predict a large (3–4 km) depression in dynamic topography on the overriding plate (in the arc/back arc region) and a short wavelength depression in the geoid or gravity over the back arc region. Billen and Gurnis [in press] [Chapter 3] demonstrated that this deep basin can be eliminated by including a low viscosity region in the wedge, thereby decoupling the flow of the slab from the overriding plate.

4.2.3 Seismological Constraints on Viscosity

The viscous strength of the slab is an important parameter coupling flow in the mantle to the observed deformation on the surface. However, it is difficult to isolate the viscosity of the slab from other viscosity variations using only topography and geoid, nor is it possible to infer the absolute viscosity of the slab. Several dynamic studies have concluded that the lithosphere weakens as it bends at the trench and subducts into the mantle [Conrad and Hager, 1999; Zhong et al., 1996]. However, the occurrence of seismicity within slabs to depths of 670 km implies that the slab retains some strength throughout the upper mantle. Observations of strain-rates and stress orientations inferred from seismicity and moment tensor solutions provide additional constraints on the strength of slabs and coupling of slabs to the higher viscosity lower mantle.

Earthquakes provide an indirect measure of the strain release within areas of distributed deformation and a lower bound on the strain-rate within the interior of the earth. The strain-rate $\dot{\epsilon}$ due to earthquakes can be estimated as $\dot{\epsilon} = \sum M_o/2\mu V t$, where $M_o = \mu A D$ is the moment for a single earthquake (μ is the elastic shear modulus, A is the area of the fault, D is the average slip over A) and $\sum M_o$ is the cumulative seismic moment release within a volume V, occurring over a timespan t [Kostrov, 1974]. Bevis [1988] used this model of strain-rate release from earthquakes to estimate the strain-rate in slabs to be on the order of $1{\times}10^{-15}$ s^{-1} between 75 and 175 km. Holt [1995] and Nothard et al. [1996] found similar strain-rates for a portion of the Tonga slab down to 200 km depth with slightly smaller strain-rates

($5\times10^{-16}\ s^{-1}$) between 200 and 650 km. These estimates of the minimum strain-rate in the slab provide an important constraint on the viscosity of the slab in dynamic models.

The orientation of stress within slabs based on compressional and tensional axes of earthquake focal mechanisms provides another constraint on the strength of slabs and the lower mantle. Most slabs with seismicity extending to 670 km depth are in down-dip or vertical tension in the upper 300 km and compression below 300 km [Isacks and Molnar, 1971]. The Tonga-Kermadec and Izu-Bonin slabs are important exceptions, which appear to be in down-dip compression throughout [Isacks and Molnar, 1971; Apperson and Frohlich, 1987; Seno and Yamanaka, 1998]. Vassiliou et al. [1984] showed that the stress orientations and distribution of number of earthquakes with depth, at most subduction zones, is consistent with a slab sinking under its own weight and meeting a substantial resistance to flow at a depth of 670 km: a gradual decrease from the surface to 300 km, a minimum between 300 and 400 km and an increase from 400 to 670 km. Regional studies have shown that seismic strain-rate [Holt, 1995; Nothard et al., 1996] has the same depth distribution within the slab.

4.3 The Subduction Zone Wedge

The wedge in a subduction zone, the region above a subducting plate and beneath the overriding plate, is likely the location of strong lateral variations in viscosity and buoyancy due to processes involving fluids released by the subducting slab and subsequent metasomatism and melting. Previous models have incorporated the exponential dependence of viscosity on temperature, the pressure and mineralogical variations in viscosity in terms of radially stratified viscosity structure and stress-dependent viscosity in terms of non-Newtonian flow laws. However, the influence of melt and water on viscosity has largely been ignored due to the challenges in explicitly including such variations and lack of experimental and theoretical constraints on its influence. However, Davies and Stevenson [1992] demonstrated that local variations in viscosity or buoyancy may strongly affect flow in the wedge.

4.3.1 Evidence of a Low Viscosity Wedge

Recently, experimental and theoretical research on the rheological behavior of olivine at conditions applicable to the upper mantle has made it possible to use seismic observations to constrain the location of fluids in the upper mantle and begin to quantify the effects of these fluids on viscosity.

Geochemical and petrologic data indicate that fluids are incorporated into the wedge due to dehydration of the subducting slab [Tatsumi et al., 1983; Stolper and Newman, 1994; Morris et al., 1990]. Tatsumi et al. [1983] found that the chemical composition of primary magmas for the N. E. Japan arc formed in the presence of 3 wt% water. Stolper and Newman [1994] explained the composition of Mariana trough and island arc magmas in terms of mixing of a NMORB source (infertile peridotite) with an H_2O-rich component, and attributed the increase in degree of melting from the back arc to the island arc as due to an increase in the amount of water in the wedge closer to the island arc. Morris et al. [1990] showed that the source for water in island arc magmas is water carried down by the slab by tracing the elements B and Be in the magmas to sediments on the down-going plate.

Experimental studies of rheology at low pressures (< 300 MPa) show that the viscosity of olivine aggregates decreases approximately linearly with increasing water content [Mei, 1999; Karato, in press]. While the rheology of minerals at higher pressures has been poorly constrained, a recent study at 2 GPa has established a quantitative flow law for olivine that can be extrapolated to higher pressure [Karato and Jung, submitted]. This work, combined with the results on pressure dependence of hydroxyl solubility in olivine [Kohlstedt et al., 1996], suggests that the weakening effects of water will be even greater at the higher water fugacity conditions likely in the deep upper mantle of a subduction zone.

Seismic studies in subduction zones reveal anomalies of low velocity [Hasegawa et al., 1991; Roth et al., 2000] and high attenuation [Roth et al., 2000; Barazangi and Isacks, 1971] in the wedge, consistent with the presence of volatiles, particularly water [Karato and Jung, 1998] and possibly melt. Tomography studies for the N. E. Japan subduction zone reveals a -4% to -6% P-wave velocity anomaly in the upper-most mantle, immediately beneath the arc crust, which is continuous along the strike of the arc [Zhao et al., 1992]. Similar anomalies of -2% to -6% are found in regional tomography models of the Tonga-Kermadec subduction zone [Zhao et al., 1997]. Observations of high attenuation (low Q) accompany observations of low seismic velocity in N. E. Japan and Tonga-Kermadec [Barazangi and Isacks, 1971; Roth et al., 1999]. For Tonga-Kermadec, attenuation within the wedge increases with $Q = 70$–150 compared to a reference value for P-waves in the asthenosphere of $Q_o = 200$ [Dziewonski and Anderson, 1981]. While resolution in attenuation models is much less than in seismic velocity models, regions of high attenuation (low Q) and low seismic velocity appear to be correlated in these subduction zones. Using the results of Karato [in press] the low seismic velocity (-4% to -6%) and high attenuation regions found above the N. E. Japan and Tonga-Kermadec slabs indicate water concentrations of at least 3000 H/10^6 Si, if the associated temperature anomalies are $\sim$200 K. These water concentrations are three times those inferred for the oceanic asthenosphere under mid-ocean ridges.

In addition to experimental evidence for the weakening effects of water at relatively low pressures, Karato [in press] presents a relationship between viscosity and seismic attenuation and velocity. This relationship, which assumes that the kinetics of both attenuation and steady-state creep are affected by water through the same mechanism (i.e., weakening due to hydrogen-related defects), provides a quantitative method by which seismic observations can be used to map the viscosity structure of the mantle. For the low seismic velocity (-2% to -5% for P-waves) and high attenuation regions of the wedge, this relationship predicts a decrease in viscosity of 2–4 orders of magnitude.

At shallow depths in the wedge ($<$ 100 km), observations of low seismic velocity are more likely due to relatively high melt fraction beneath the active island arc. In mid-ocean ridge environments the low water content and low pressures of melting lead to an increase in viscosity in the residue of melting as water is fully partitioned into the melt and the melt fraction is not high enough to decrease the viscosity [Hirth and Kohlstedt, 1996]. Depending on the degree of melting and flux of volatiles from the subducting slab, experimental evidence on the influence of melt on the rheology of olivine aggregates indicates that, where there is high melt fraction, the viscosity of the mantle decreases exponentially with increasing melt content [Kelemen et al., 1997]. Therefore, these shallow low velocity regions may also be low viscosity regions.

These observations and experiments suggest the viscosity in the wedge extending from the top of the subducted slab at depths of 100–200 km to the base of the overriding crust may be substantially less than the background asthenosphere and mantle lithosphere. Such a low viscosity wedge (LVW) will affect the flow in the wedge and deformation of the overriding plate.

4.3.2 Sources of Buoyancy in the Wedge

Density variations within the wedge may result from the processes associated with extensive fluxing of volatiles from the slab, induced melting beneath the back arc and island arc, and subsequent depletion of the source region for magmas. The main effect of water fluxing into the wedge is to increase the degree of melting by decreasing the solidus temperature. Above the wet solidus, in regions of high melt fraction, the density in the wedge may decrease by 5–20 kg/m^3 for an in-situ melt fraction of 1–4% (the density of the melt, ignoring variations with depth, will be approximately 500 kg/m^3 less than the surrounding rock). Continual fluxing of water into the wedge also leads to larger degrees of melting and can lead to a decrease in density of the residue remaining in the wedge. Stolper and Newman [1994] found that the degree of melting increased from 5–17 wt% for the Mariana back arc to greater than 30 wt% for island arc magmas. Such high degrees of melting lead to lower Al_2O_3 contents in the residue. At low pressures ($P < 10$ kbar), in the spinel stability field, this leads to little change in density. However, if this residue is transported into the garnet stability field ($P > 30$ kbar) by flow in the wedge, the low Al_2O_3 content limits the amount of garnet that forms. This results in a 10–20 kg/m^3 decrease in the density relative to peridotite that has undergone only 10 wt% melting and a density decrease of up to 50 kg/m^3 compared to fertile peridotite (P. Asimow, personal communication).

While density variations in the crust or at the base of the crust due to melt will contribute to dynamic topography, these variations are isostatically compensated and therefore do not significantly contribute to the geoid or gravity. Density anomalies in the deeper (100–200 km) regions of the wedge due to extensive depletion of peridotite will contribute to both dynamic topography and the geoid.

4.4 Numerical Method

We develop a model of instantaneous dynamic flow which allows us to focus on the effects of lateral variations in viscosity on deformation in a subduction zone. From the velocity and pressure we calculate topography, geoid, stress orientations and strain-rates to characterize those viscosity structures that are consistent with the general form of deformation observed at the world's subduction zones and the particular case of the Tonga-Kermadec subduction zone.

Flow in the mantle is governed by the equations for conservation of mass and momentum. For the mantle, with a very high Prandtl number, inertial forces are negligible. We use the Boussinesq approximation which ignores all variations in density except in the body force term in the momentum equation. With these assumptions the equations for conservation of mass and momentum reduce to the continuity equation,

$$\nabla \cdot \mathbf{u} = 0 \tag{4.1}$$

and the Stokes Equation,

$$\nabla \cdot \sigma + \mathbf{f} = 0 \tag{4.2}$$

where $\mathbf{u}$, $\mathbf{f}$ and σ are the flow velocity, the body force and stress tensor, respectively. The body force includes density anomalies due to temperature T (inferred density variations due to composition of the crust are included in terms of equivalent temperature),

$$f_i = \rho_o \alpha (T - T_o) g \delta_{ir} \tag{4.3}$$

where ρ_o is the reference density, T_o is reference temperature, g is the gravitational acceleration, α is the coefficient of thermal expansion and δ_{ij} is Kronecker delta.

The stress tensor defines the constitutive relation

$$\sigma_{ij} = -P\delta_{ij} + \eta \dot{\epsilon}_{ij} \tag{4.4}$$

where P is the pressure, η is the dynamic viscosity, and $\dot{\epsilon}_{ij}$ is the strain-rate tensor in spherical coordinates given by

$$\dot{\epsilon}_{ij} = (u_{i,j} + u_{j,i}) \tag{4.5}$$

where $u_i \equiv (u_\phi, u_r, u_\theta)$, $X_{,y}$ denotes the derivative of X with respect to y, i and j are spatial indices and the spatial coordinates (x_i) are longitude ϕ, radius r and latitude θ. Making the following change of variables

$$\begin{gathered} x_i = Rx'_i \quad u_i = \tfrac{\kappa}{R}u'_i \\ P = \tfrac{\eta_o\kappa}{R^2}P' \quad \eta = \eta_o\eta' \\ T = T_o + \Delta T T' \end{gathered} \tag{4.6}$$

where R is the radius of the Earth, κ is the thermal diffusivity, η_o is the reference viscosity and ΔT is the temperature difference between the top surface and the interior of the mantle, and substituting Equations 4.3 and 4.4 into Equation 4.2, the equations of motion become

$$u'_{i,i} = 0 \tag{4.7}$$

and

$$-P'_{,j}\delta_{ij} + (\eta' u'_{i,j} + \eta' u'_{j,i})_{,j} + RaT'\delta_{ir} = 0 \tag{4.8}$$

where

$$Ra = \frac{\rho_o g \alpha \Delta T R^3}{\eta_o \kappa} \tag{4.9}$$

is the Rayleigh number which depends on the choice of physical parameters for the Earth's mantle.

The choice of η_o is not immediately obvious for a fully three-dimensional viscosity structure. The Stokes Equation expresses a balance of buoyancy and viscous forces which depends on the velocity. In this balance the magnitude of the velocity scales inversely with η_o while the distribution of flow and pressure will depend only on relative viscosity within the model. Since our aim is to study variations in the viscosity structure, it is important to choose η_o to coincide with a region for which the viscosity is the same for all the models so that comparisons of stress and topography are

Table 4.1: Model Parameters

Variable Name		**Value**
Reference density	ρ_o	3300 kg/m^3
Temperature difference between the top and bottom surface	ΔT	1500 K
Thermal diffusivity	κ	1×10^6 m^2/s
Coefficient of thermal expansion	α	2×10^{-5} K^{-1}
Earth radius	R	6371.137 km
Gravitational acceleration	g	10 m/s^2
Reference viscosity	η_o	3×10^{20} Pa s
Rayleigh number	Ra	8.53×10^8

straightforward. We choose to have η_o coincide with the asthenosphere viscosity η_{asth}. Implicit in this choice is the assumption that the viscosity of the asthenosphere is important in determining the magnitude of flow in the upper mantle and in particular in the slab.

The values for the physical parameters used in most of the models are summarized in Table 4.1. For models in which other parameters are used, the differing parameters will be indicated. The viscosity is radially, laterally and temperature dependent. Radially, the mantle is divided into four layers: lithosphere (0–100 km), asthenosphere (100–410 km), transition zone (410–670 km) and the lower mantle (670–2890 km). The temperature dependence of the non-dimensional viscosity in each layer is given by

$$\eta'(r', T') = \eta^*(r, \phi, \theta) \exp\left(\frac{c_1}{T' + c_2} - \frac{c_1}{1 + c_2}\right) \tag{4.10}$$

where the constants c_1, c_2 and $\eta^*(r, \theta, \phi)$ can differ in each layer. Lateral variations in viscosity not due to temperature variations are included by setting c_1 and c_2 to zero and η^* to the desired viscosity.

4.4.1 Model Domain and Boundary Conditions

The equations of motion are solved for the velocity and pressure by the finite element code **CitcomT**, designed to study 3-D dynamic models in a region of a sphere. **CitcomT** has been modified from the Cartesian geometry code **Citcom** [Moresi and

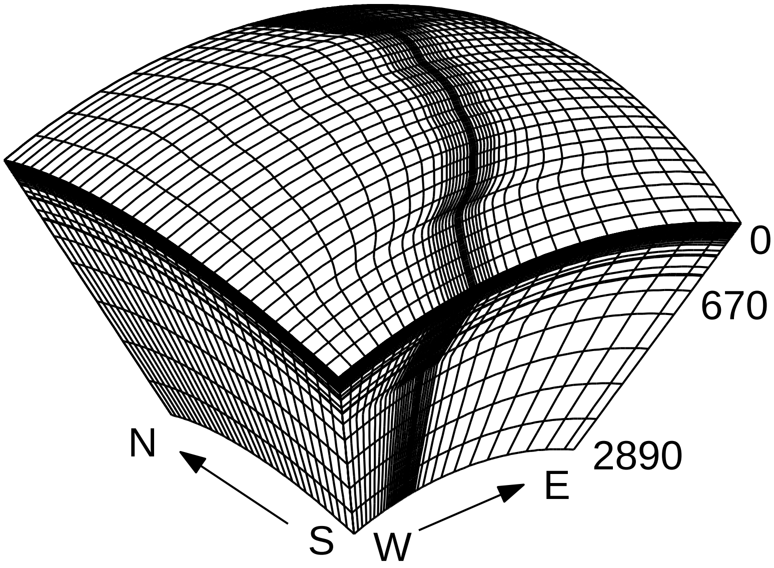

Figure 4.3: A 3-D view of the mesh and model domain. The model domain extends from the surface to the core-mantle boundary, -5° to -50° in latitude and 155° to 200° in longitude. The mesh boundaries displayed are sampled at every third row of nodes. The mesh has uniform spacing in latitude every 0.5°. Resolution in depth varies from 2.5 km near the surface to 100 km below 670 km, with increased resolution at 410 and 670 km depth. Resolution in longitude ranges from 2.5 km near the fault and slab to 100 km at the east and west boundaries of the domain. The high resolution regions follow the contours of the slab in depth and latitude.

Solomatov, 1995; Moresi and Gurnis, 1996; Zhong et al., 1998] using a coordinate transformation to spherical geometry (see Appendix A). The model domain extends from the surface to the core-mantle boundary (Figure 4.3). Three-dimensional models of the Tonga-Kermadec region extend 45° in longitude (155°–200°) and latitude (5°S–50°S) where the side-walls of the domain are lines of equal longitude or latitude. The top and bottom surfaces have free-slip ($u_{rr} = 0$, $\sigma_{r\theta} = \sigma_{r\phi} = 0$), isothermal boundary conditions. The side-walls have reflecting boundary conditions ($u_{\theta\theta} = 0$ or $u_{\phi\phi} = 0$). Two-dimensional models used for investigating the general behavior of the flow with lateral variations in viscosity are taken from a 2-D cross section through the 3-D model at a latitude of 28°S. A fault along the subduction zone boundary within the lithosphere is modeled with boundary conditions requiring continuous normal stress on the fault interface but allowing discontinuous tangential stresses.

The fault interface lies along a single plane of element boundaries within the mesh. The varying strike and dip of the fault in 3-D requires that this surface of elements is deformed to match the fault geometry. In addition, modeling with strong variations in viscosity over short length-scales requires the mesh to have high resolution in these regions. Viscosity variations across a single element are constrained to be less than a factor of 3 for numerical accuracy. Moresi et al. [1996] found that accuracy does not depend on the global viscosity variation but rather on gradients within individual elements: accuracy falls below 1% if viscosity varies by more than a factor of two or three in an element. This means that an order of magnitude variation in viscosity is spread across three elements. To facilitate viscosity variations of several orders of magnitude over a few tens of kilometers, we use a mesh with resolution that varies from 2.5–100 km with the highest resolution in the wedge and along the top surface of the slab.

4.4.2 Density Structure

The main driving force for deformation in the subduction zone is the negative buoyancy of the slab. However, other density anomalies, due to variations in the age of the lithosphere, crustal thickness, phase change boundaries and compositional differences, may also have an important influence on the flow, topography and geoid. The slab buoyancy in our models is derived from a kinematic model of flow constrained to follow the location of the slab delineated by seismicity from the surface to a depth of ∼670 km (see Appendix D). The maximum density anomaly within the slab is ∼66 kg/m^3 (using the parameters in Table 4.1). It is important to include variations in the age of the lithosphere and crustal thickness since the density anomalies associated with both of these variations can contribute to isostatically compensated topography and dynamic topography through induced flow. Age variations within the Tonga-Kermadec model range from 0 Ma along the active back arc spreading system in the Lau and Havre basins to greater 100 Ma on the Pacific Plate. Figure 4.4A shows the ages based on well-recognized magnetic anomalies [Müller et al., 1997]. In Figure 4.4B, the ages for the overriding plate are extrapolated based on the presence of active spreading centers (Lau Basin, Havre Trough, North Fiji Basin) and tectonic history [Kroenke, 1984]. Ages on the subducting Pacific Plate east of the Tonga-Kermadec Trench are based on the age of the Osbourn Trough, an extinct spreading center which may have stopped spreading as recently as 72 Ma (Chapter 1). Ages to the north and sourth of the Osbourn Trough are estimated based on a 2.5 cm/yr average spreading rate for the Osbourn Trough before it stopped spreading. In areas where the age is not known we assign an age of 80 Ma. This value is also assigned to a 500 km wide border along the edges of the model domain (not shown) to avoid offsets in topography across the model boundary in the geoid calculation. Crustal thickness variations for the continental region (New Zealand, Chatham Rise, Campbell Plateau and Lord Howe Rise), remnant arc (Coleville Ridge) and active Tonga-Tofua Arc [Raitt et al., 1955] are also included in the 3-D models. We do not include density variations due to the phase changes at 410 and 670 km. Recent studies suggest that the cold temperature within the slab may inhibit the transformation of olivine to spinel at 410 km leading to little net change in density or a decrease in the density of the slab relative to the mantle [Stein and Stein, 1996]. In addition, as we will discuss later, we find that the density of the slab due to temperature may be too high to match observations of the geoid, and the exothermic phase change at 410 km will only further increase the discrepancy we find. The final source of density variations is compositional difference within the mantle. By compositional density anomalies we are including the many processes in the mantle wedge which may lead to differences in the density of the wedge: the presence of melt, compositional changes due to extensive melting and the presence of water (see Section 4.3.2). We do not attempt to include the processes that lead to the density variations. Instead we focus on how the density variations resulting from these processes might influence the flow, surface deformation and the geoid.

4.4.3 Surface Observables

The topography, geoid and gravity are determined from the non-dimensional velocity and pressure. The non-dimensional dynamic topography h' on the top or bottom surfaces balances the normal stress on that surface,

$$h' = \sigma'_{rr}. \tag{4.11}$$

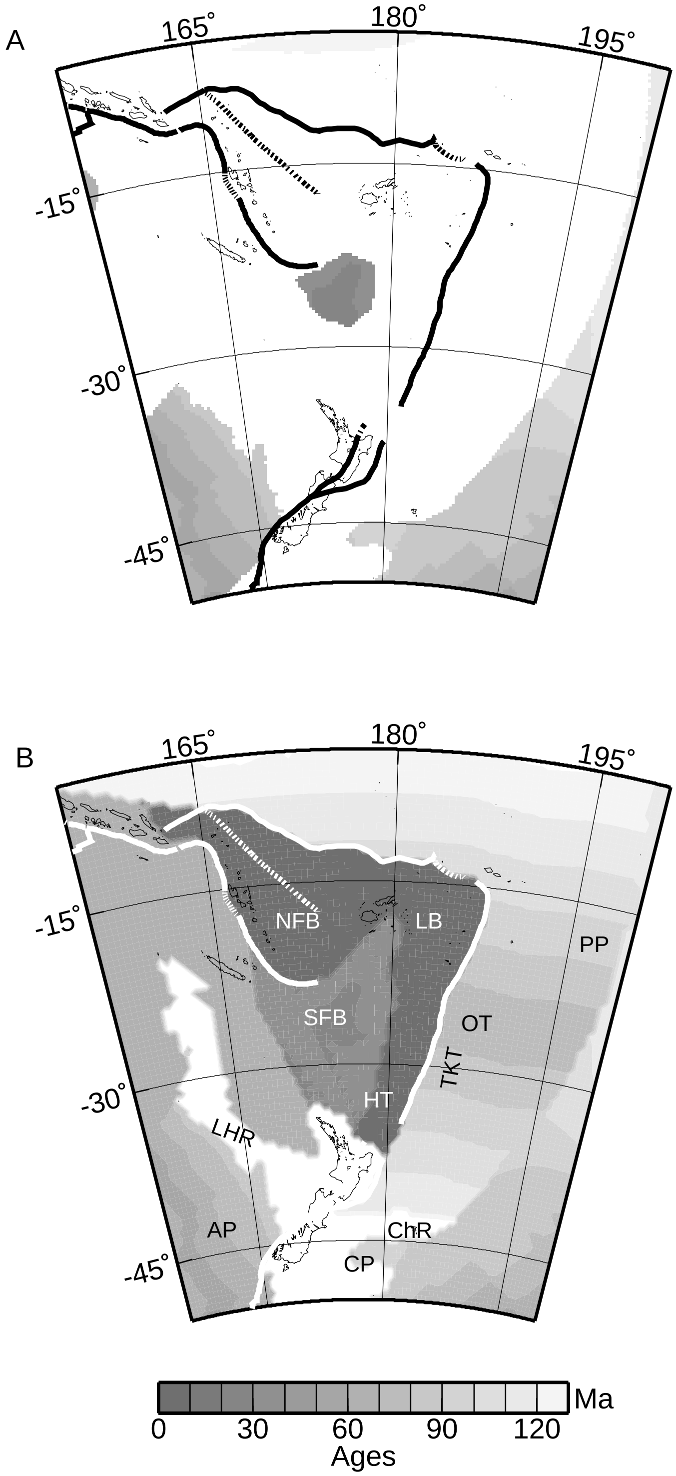

Figure 4.4: **A.** Age of the seafloor within the model domain known from well recognized magnetic anomalies [Müller et al., 1997]. **B.** Age of the seafloor from location of known active back arc spreading centers, tectonic history and the age of the Osbourn Trough. White regions indicate continental crust. Location labels are the same as Figure 4.2; OT, Osbourn Trough.

where $\sigma_{rr} = \frac{\eta_o \kappa}{R^2}\sigma'_{rr}$. To dimensionalize the dynamic topography we assume that the surface is everywhere covered by water (this underestimates the topography over the continents which reach above sea-level), then

$$h = \frac{\eta_o \kappa}{\Delta \rho g R^2}\sigma'_{rr} \tag{4.12}$$

where $\Delta\rho = \rho_o - \rho_w = 2300$ kg/m^3 is the density contrast between the lithosphere and the water.

Accurate determination of dynamic topography is especially important in determining the geoid and gravity which depend on the small difference in the potential due to density anomalies in the interior of the model and density anomalies due to surface deformation. Extensive testing of the topography calculation demonstrates that the topography is accurately determined, with errors less than 1% in the presence of strong radial or lateral variations in viscosity (Appendix B).

An important constraint on the validity of our dynamic models is agreement with the observed geoid height, N or gravity anomaly, δg. The observed geoid height and gravity anomaly are commonly expressed in terms of coefficients of a finite sum of surface spherical harmonic functions. In the case of the observed geoid and gravity, these coefficients are inverted directly from orbital data of satellites [Lambeck, 1988]. Several techniques for comparing model geoid and gravity take explicit advantage of the spherical harmonic representation of these fields. Therefore, we solve directly for the harmonic coefficients of the geoid height (or gravity anomaly) due to density anomalies within the model domain,

$$N^i_{lm} = \int_\Omega \left(\frac{\gamma}{gR}\right) \frac{\delta\rho(r,\lambda,\phi)}{2l+1} \left(\frac{r}{R}\right)^l Y^i_{lm}(\lambda,\phi) d\Omega, \tag{4.13}$$

and resulting topography on the surface and core-mantle boundary (see Appendix C for a full description),

$$N^i_{lm}(h) = \int_S \left(\frac{\gamma}{gR}\right) \frac{h(\lambda,\phi)\Delta\rho}{2l+1} \left(\frac{r}{R}\right)^l Y^i_{lm}(\lambda,\phi) dS \tag{4.14}$$

where λ is colatitude, $d\Omega = r^2 \cos(\lambda)\partial\lambda\partial\phi\partial r$, $dS = r^2\cos(\lambda)\partial\lambda\partial\phi$, $Y^i_{lm}(\lambda,\phi)$ is the surface spherical harmonic functions, l and m are the degree and order of the spherical harmonic, i refers to the *sine* or *cosine* term of the ϕ dependence and γ is the gravitational constant. $\delta\rho(r, \lambda, \phi)$ is the density anomaly within the domain. For the contribution due to topography (h_t on the top surface or h_b at the core-mantle boundary), $\delta\rho(r, \lambda, \phi)dr$ is replaced by $h(\lambda, \phi)\Delta\rho$ for that boundary. The total geoid at a point on the surface (λ_1, ϕ_1) is given as the sum of three contributions,

$$N(R, \lambda_1, \phi_1) = \sum_{lmi} \left[N^i_{lm} + N^i_{lm}(h_t) + N^i_{lm}(h_b)\right] Y^i_{lm}(\lambda_1, \phi_1) \tag{4.15}$$

A similar expression for the gravity anomaly is found by substituting $(l + 1)/r$ for $1/g$ in Equations 4.13 and 4.14.

The spherical harmonic functions used in calculating the geoid and gravity are defined for a whole sphere. Therefore, using these functions to calculate the geoid or gravity within our regional domain implicitly assumes that there are no density anomalies outside our domain. This mean that if there are density anomalies or non-zero topography along the boundaries of the model, there is in effect a step discontinuity along the boundary which would lead to a large short wavelength signal in the geoid or gravity. To avoid this contamination of the predicted geoid and gravity, we taper density anomalies to zero at 500 km from the domain boundaries (age of the lithosphere along the boundary is set to 80 Ma) and the topography is shifted by the mean value along the edge of the domain to minimize any offset across the model boundaries prior to computing the geoid height.

4.5 2-D Models of Subduction Zone Dynamics

We begin by exploring the influence of both radial and lateral variations in viscosity on topography, velocity, strain-rate and stress orientation, in 2-D generic models of instantaneous dynamic flow in a subduction zone. The results are first presented in Section 4.5.1 for models with only radial- and temperature-dependent viscosity (i.e., all lateral variations in viscosity are due to temperature). These models are listed in Table 4.5. A subset of these models, including a low viscosity and buoyant region in the wedge, is further investigated in Sections 4.5.2 and 4.5.3, respectively.

Table 4.5: 2-D Radial and Temperature Dependent Viscosity Models

Model	$\frac{\eta_{slab}}{\eta_o}$	$\frac{\eta_{lith}}{\eta_{slab}}$	$\frac{\eta_{lm}}{\eta_{slab}}$	$\frac{\eta_{tran}}{\eta_{lm}}$	h_{basin} **(km)**	h_f **(km)**	$\dot{\epsilon}$ **(s^{-1})**	M
1a	0	2	2	-2	-6.51	0.0	2.6×10^{-14}	8.84
1b	1	1	1	-2	-6.67	0.0	4.6×10^{-15}	37.01
1c	2	0	0	-2	-7.40	0.05	9.6×10^{-16}	70.10
2a	0	3	2	-2	-6.78	0.0	2.5×10^{-14}	1.05
2b	1	2	1	-2	-7.22	0.0	4.2×10^{-15}	5.65
2c	2	1	0	-2	-8.56	0.0	8.1×10^{-16}	21.46
2d	3	0	-1	-2	-11.37	0.10	1.9×10^{-16}	49.15
3a	0	4	2	-2	-6.91	0.0	2.4×10^{-14}	0.11
3b	1	3	1	-2	-7.35	0.0	4.1×10^{-15}	0.65
3c	2	2	0	-2	-8.82	0.0	7.8×10^{-16}	2.84
3d	3	1	-1	-2	-11.92	0.0	1.9×10^{-16}	9.11
3e	4	0	-2	-2	-15.93	0.77	3.7×10^{-17}	16.51
4a	1	1	1	-1	-6.34	0.0	3.8×10^{-15}	41.35
4b	2	0	0	-1	-6.95	0.01	8.4×10^{-16}	77.72
5a	1	2	1	-1	-7.10	0.0	3.6×10^{-15}	6.66
5b	2	1	0	-1	-8.31	0.0	7.1×10^{-16}	25.11
5c	3	0	-1	-1	-11.00	0.03	1.8×10^{-16}	54.13
6a	1	3	1	-1	-7.26	0.0	3.4×10^{-15}	0.76
6b	2	2	0	-1	-8.65	0.0	6.9×10^{-16}	3.41
6c	3	1	-1	-1	-11.60	0.0	1.7×10^{-16}	10.49
6d	4	0	-2	-1	-15.50	0.63	3.5×10^{-17}	18.00
7a	2	0	0	0	-6.47	0.05	7.2×10^{-16}	80.44
8a	2	1	0	0	-8.07	0.0	6.4×10^{-16}	28.23
8b	3	0	-1	0	-10.55	0.0	1.7×10^{-16}	59.36
9a	2	2	0	0	-8.50	0.0	6.3×10^{-16}	3.97
9b	3	1	-1	0	-11.30	0.0	1.5×10^{-16}	12.65
9c	4	0	-2	0	-14.88	0.44	3.1×10^{-17}	21.88
10a	2	2	-1	-1	-10.51	0.0	1.4×10^{-15}	1.35
10b	3	1	-2	-1	-13.79	0.36	2.8×10^{-16}	2.70
10c	4	0	-3	-1	-19.21	2.39	5.3×10^{-17}	5.78
11a	2	2	-2	0	-11.12	0.05	1.7×10^{-15}	0.53
11b	3	1	-3	0	-15.07	1.33	3.5×10^{-16}	1.15
11c	4	0	-4	0	-21.76	4.50	6.7×10^{-17}	3.73
4ayl	1	1	1	-1	-7.11	0.13	4.2×10^{-15}	40.97
4byl	2	0	0	-1	-8.16	0.35	8.6×10^{-16}	79.52
5ayl	1	2	1	-1	-8.69	0.01	3.9×10^{-15}	6.91
5byl	2	1	0	-1	-11.59	0.19	7.6×10^{-16}	25.93
5cyl	3	0	-1	-1	-16.13	0.74	1.8×10^{-16}	55.72
6ayl	1	3	1	-1	-9.67	0.0	3.8×10^{-15}	0.89
6byl	2	2	0	-1	-13.48	0.07	7.5×10^{-16}	3.73
6cyl	3	1	-1	-1	-20.78	0.73	1.8×10^{-16}	11.18
6dyl	4	0	-2	-1	-26.47	2.41	3.9×10^{-17}	17.85
12	2	0	0	-1	-7.5	0.03	1.6×10^{-16}	54.05
13	3	0	-1	-1	-6.0	0.0	8.9×10^{-16}	73.69

See caption, next page.

4.5.1 Radial and Temperature Dependent Viscosity Models

For models with radial and temperature dependence there are five independent viscosity parameters: lithosphere (η_{lith}), slab (η_{slab}), asthenosphere (η_{asth}), transition zone (η_{tran}) and lower mantle (η_{lm}) viscosity. As stated earlier, the asthenosphere viscosity is the reference viscosity (η_o), therefore all viscosity values are scaled by this value. This is an important point: velocity (and strain-rate) depends on η_o and is sensitive to both the absolute and relative values of the viscosity in the model. However, the pressure (stress and topography) does not depend directly on η_o and is therefore only dependent on the relative variations of viscosity within the model. The models presented use a reference viscosity of 3×10^{20} Pa s unless otherwise noted. The lithosphere, slab, transition zone and lower mantle viscosity vary over several orders of magnitude (Table 4.5). We limit the number of possible models by requiring that: $\eta_{slab} \geq \eta_{tran}$, $\eta_{slab} \leq \eta_{lith}$ and $\eta_{tran} \leq \eta_{lm}$, consistent with previous results for the radial viscosity structure of the mantle [King, 1995]. In addition to the effects of temperature dependent viscosity associated with the slab, we investigate the influence of the age of the overriding plate which contributes to lateral variations in viscosity due to variation in lithosphere thickness.

Basin Depth. As found previously [Zhong and Gurnis, 1992, 1994; Zhong et al., 1998; Moresi and Gurnis, 1996], a large basin forms on the overriding plate for all models with only radial- and temperature-dependent viscosity (Table 4.5), with depths varying from 6 to 26 km. We find that the basin depth increases with increasing strength of the slab (Figure 4.5). This increase in basin depth is independent of all other viscosity parameters including lithosphere viscosity. The dependence of the dy-

Table 4.5 Model viscosity parameters are relative to the reference viscosity (η_o): values listed are $\log_{10}$ for each ratio. h_{basin} is depth of the basin on the overriding plate and h_f is fore-arc height and $\dot{\epsilon}$ is the volume averaged second-invariant of the strain-rate tensor within the slab below 100 km. M is the plate mobility defined in the text. Models 1a–11c: $\eta_o = 3\times10^{20}$ Pa s, Ra $= 8.58\times10^{8}$, lithosphere age is 50 myr. Models 4ayl–4byl: $\eta_o = 3\times10^{20}$ Pa s, Ra $= 8.58\times10^{8}$, lithosphere age is 0–100 Ma. Model 12: $\eta_o = 3\times10^{21}$ Pa s, Ra $= 8.58\times10^{7}$, lithosphere age is 50 Ma (compare to 5c). Model 13: $\eta_o = 3\times10^{19}$ Pa s, Ra $= 8.58\times10^{9}$, lithosphere age is 50 Ma (compare to 4b).

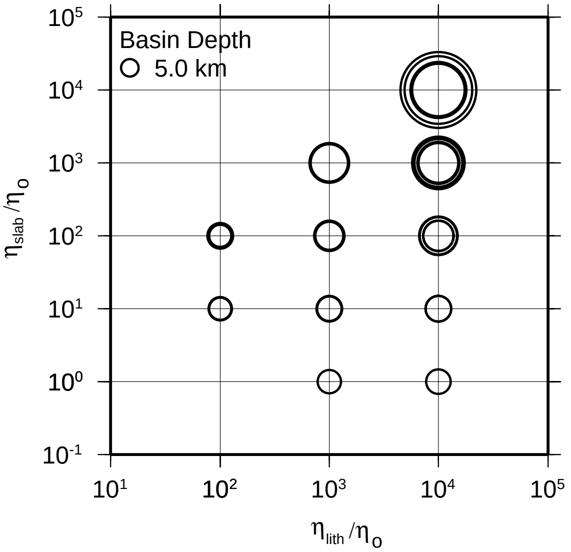

Figure 4.5: Basin depth dependence on η_{slab}/η_o and η_{lith}/η_o for models 1a–11c. Basin depth, indicated by the circle size, increases with increasing η_{slab}/η_o, but shows no dependence on η_{lith}/η_o or other viscosity variables.

namic topography of the overriding plate on the slab viscosity can be understood by examining the balance between the flow and pressure above the slab. Sinking of the dense slab creates a region of low pressure above the slab and high pressure below the slab. (Note that pressure is only known to within an arbitrary constant, so we only know the relative magnitude of the pressure). Low pressure corresponds to suction into the region which pulls down on the surface to form the basin. The magnitude of the low pressure region above the slab depends on the relative viscosity of the slab and overlying asthenosphere and the density of the slab. In all these models the density of the slab is fixed therefore, larger slab viscosity relative to the asthenosphere leads to lower pressures above the slab, reaching the surface and therefore a larger basin.

Forebulge. A forebulge on the downgoing plate, ranging in size from ~100 m to greater than 4 km, forms in two cases. First, for models with a strong lower mantle (η_{lm}/η_o = 100), a forebulge forms when the slab and lithosphere viscosity are equal (Figure 4.6). Second, a forebulge forms in all models with either a weak (10×) or no jump in viscosity from the transition zone to the lower mantle. The forebulge forms in response to viscous flexure of the slab and lithosphere. When the slab is strongly coupled to the surface, the weight of the slab and flow in the mantle

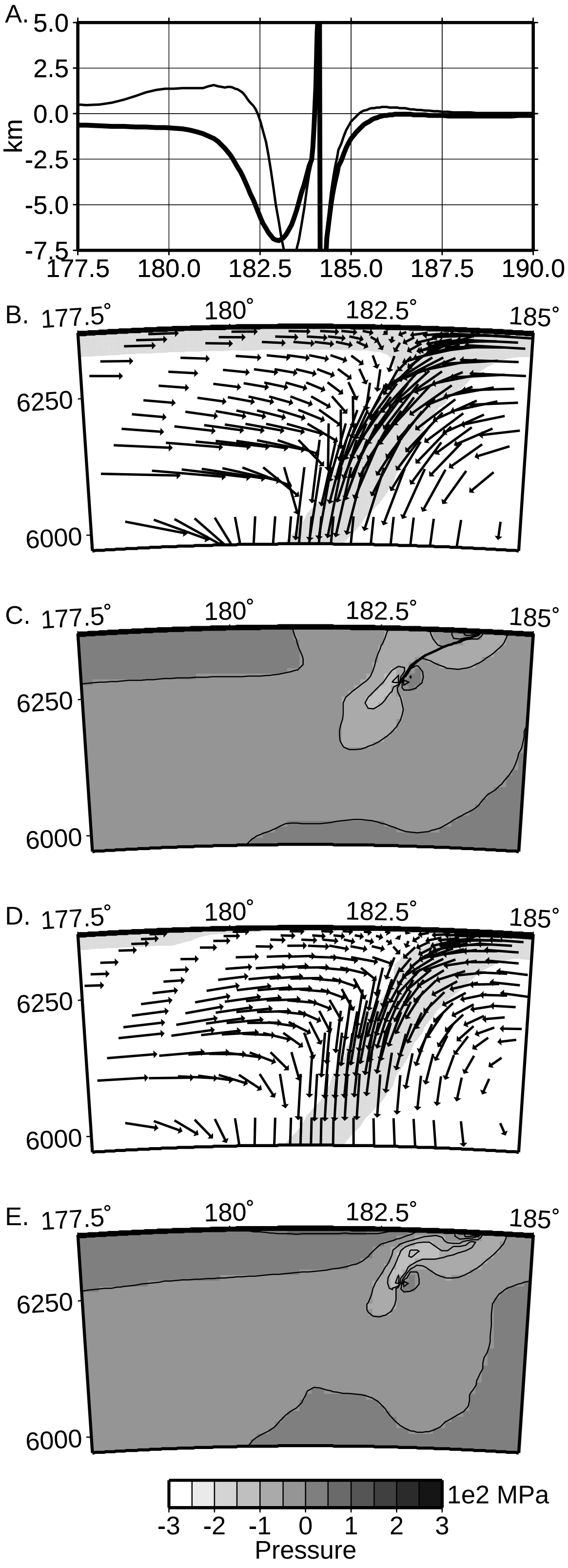

Figure 4.6: See caption next page

bend the lithosphere within the subduction zone. As in flexure of an elastic plate, viscous flexure leads to regions of horizontal compression beneath the surface of the lithosphere which is in horizontal extension. If the magnitude of the stress within the interior of the lithosphere is large enough, the overlying lithosphere is pushed up to form a forebulge outboard of the trench. In our models, forebulge heights consistent with observations (100–500 m) form when the lithosphere viscosity is relatively low ($< 1000 \times \eta_o$) and there is a strong lower mantle supporting part of the stress from the slab.

Velocity Distribution. It is well known that plate velocity within convection models depends strongly on the lithosphere viscosity. Stagnant lid convection occurs if lithosphere viscosity is too high [e.g., Torrance and Turcotte, 1971] or localized regions of weakness at plate boundaries are not included [Jacoby and Schmeling, 1982]. While the models discussed in this section do have a fault acting as a zone of weakness at the plate boundary, the velocity in the lithosphere is still strongly dependent on both the lithosphere and slab viscosity. Slab pull, from the negative buoyancy of the slab, is the force driving plate motion. In order for slab pull to be effective, the slab must be strongly coupled to the overlying plate and the velocity of the plate will be comparable to the velocity of the slab. We find that for models with a large (100×) decrease in viscosity from the lithosphere to the slab, there is little flow in the lithosphere, even though flow in the slab can exceed 15 cm/yr for some models (Figure 4.7). We quantify this effect by computing the plate mobility M which we define as

$$M = \frac{v_{lith}^{max}}{v_{slab}^{max}} \times 100. \tag{4.16}$$

$M = 100$ is perfect coupling between the lithosphere plate and the slab. The maxi-

Figure 4.6: **A.** Comparison of topography for models with (4byl, thin) and without (4b, thick) young lithosphere on the overriding plate. Note that both models have a forebulge ($\eta_{slab} = \eta_{lith}$), but the forebulge height increases in model 4byl. **B.** and **C.** Flow and pressure for model 4b. **D.** and **E.** Flow and pressure for model 4byl. Color scale for pressure is for **C** and **E** with a contour interval of 50 MPa. Location of the slab in **B** and **D** is indicated by the gray region ($T' < 0.5$). Maximum velocity is 2 cm/yr. Note that the x-axis for the topography profiles extends further east (190°) than in the cross sections (185°). See Table 4.5 for model parameters.

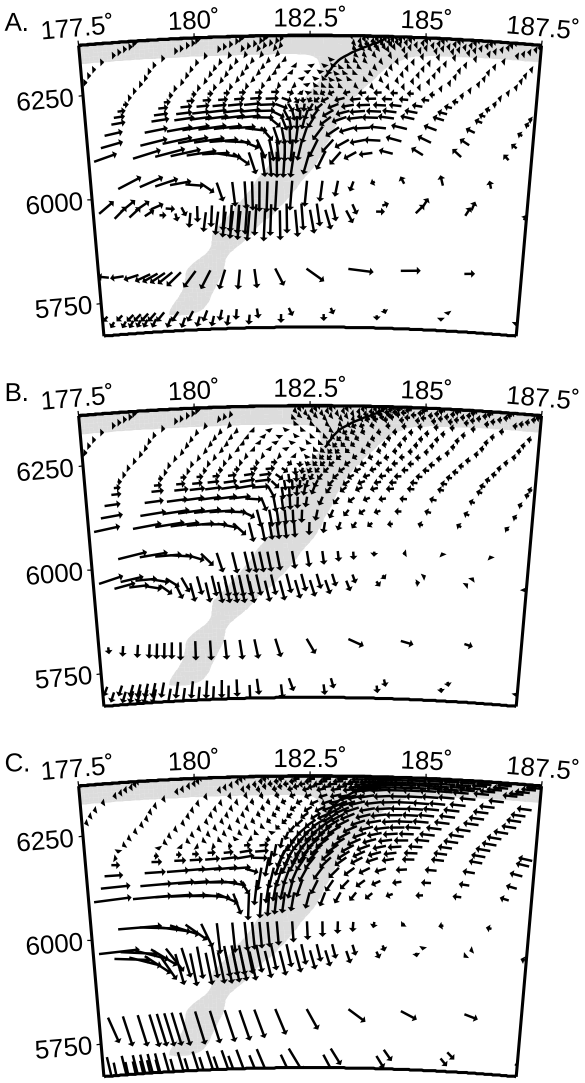

Figure 4.7: Velocity cross sections for three models with equivalent viscosity structure except for the slab viscosity in the upper mantle. **A.** model 2b, v_{max} = 3.5 cm/yr, M = 5.65. **B.** model 2c, v_{max} = 1.5 cm/yr, M = 21.46. **C.** model 2d, v_{max} = 0.5 cm/yr, M = 49.15. The velocity vectors in each cross section are scaled by the maximum so that the flow distributions can be compared. Location of the slab is indicated by the gray region ($T' < 0.5$).

mum plate mobility found in our models is for model 7a ($M = 80.44$), in which the slab and lithosphere viscosity are both $100 \times \eta_o$. This ratio may only reflect the relative viscosity of the slab and the lithosphere within the subduction zone if the plate is weakened as it nears the subduction zone. However, mobility decreases for models with higher lithosphere viscosity regardless of whether the slab and lithosphere viscosity are equal.

The viscosity of the slab also affects the flow at the bottom of the slab. Models with a strong lower mantle ($100 \times \eta_o$), and progressively stronger slabs, exhibit a rotation of the flow from vertical to oblique to the dip direction of the slab between 300 and 670 km, (Figure 4.7). The vertical flow in the weaker models (Figure 4.7A, model 2b) is driven by the negative buoyancy of the slab drawing the flow downward. Because the slab is weak ($\eta_{slab} = 10 \times \eta_o$) the upper portion of the slab simply flows (or falls) away from the lithosphere in response to the negative buoyancy of the slab beneath. Near the bottom of the slab the flow slows down and is deflected sideways by the increase in viscosity from the upper to the lower mantle. In model 2c (Figure 4.7B), the slab and lower mantle viscosity are equal ($100 \times \eta_o$) causing less deflection of the flow near the bottom of the slab. Better coupling between the slab and the lithosphere, and the increased viscosity of the slab, cause the slab to act as a stress guide to the surface. In this case rather than falling away from the lithosphere, the slab bends in response to the dense slab below. In model 2d (Figure 4.7B) this stress guide effect increases as the slab is now stronger than the lower mantle and has the same viscosity as the lithosphere. In this case there is no deflection or slowing of the flow within the slab in the transition zone and the bending of the strong slab acts as a strong boundary between flow above and below the slab.

Slab Strain-rate. Strain-rates within the slab provide a direct constraint on the absolute viscosity of the slab. As discussed earlier, the minimum strain-rate within the Tonga-Kermadec slab is estimated by the strain-rate release due to deep seismicity as 5×10^{-16} s^{-1}. We find that for models with $\eta_{slab}/\eta_o \geq 1000$, the average strain-rate in the slab deeper than 100 km is less than 5×10^{-16} s^{-1}. Therefore, the viscosity of the slab must be less than about 3×10^{23} Pa s within the upper mantle to be consistent with the observed minimum strain-rate from seismicity. This result is further verified by testing models at both higher and lower reference viscosity. Model 12 and model 5c (Table 4.5) have the same absolute viscosity for the slab ($\eta_{slab} = 3\times10^{23}$ Pa s), but model 12 has a higher reference viscosity ($\eta_o = 3\times10^{21}$ Pa s) and a lower η_{slab}/η_o ratio (100×) than model 5c (1000×). However, both have approximately the same average strain-rate in the slab ($\sim 1.8\times10^{-16}$ s^{-1}) and fail to meet the strain-rate constraint. Similarly, model 13 has a lower reference viscosity ($\eta_o = 3\times10^{19}$ Pa s) and higher

η_{slab}/η_o ratio (1000×) than model 4b (100×), but both have the same slab viscosity (3×10^{22} Pa s) and the same slab strain-rate ($\sim 8\times10^{-16}$ s^{-1}) meeting the strain-rate constraint.

In addition to the average strain-rate with the slab, the distribution of the strain-rate with depth depends on the viscosity of the slab. The observed distribution of strain-rate release from seismicity decreases with depth to 300 km, has a minimum from 300 to 400 km and increases again below 400 km. This pattern is seen in models with weaker slabs ($\eta_{slab}/\eta_o = 1$–100). For models with stronger slabs the minimum occurs between 400 and 500 km or there is no minimum. While the distribution of strain-rate is not able to distinguish between a strength-less slab and a weak slab, it does provide additional evidence that the slab is not very strong.

Stress Orientations. The orientation of stress within the slab is sensitive to both the viscosity of the slab and the change in viscosity from the upper to the lower mantle. Globally, stress orientation within slabs is observed to transition from down-dip tension to down-dip compression at around 300 km depth. We find this pattern in all models with a weak slab ($\eta_{slab}/\eta_o = 1$–100) and strong lower mantle ($\eta_{lm}/\eta_o = 100$) (Figure 4.8A, B). This pattern is caused by the upper portion of the slab falling into the mantle and pulling the overlying mantle with it, creating vertical or down-dip tension in the shallow portion of the slab. Deeper in the slab, the resistance to flow at 670 km depth is transmitted up through the slab, putting the deeper portion of the slab in compression. Strong slabs or slabs in models with a weaker lower mantle ($\eta_{lm}/\eta_o = 1$–10) are in down-dip tension throughout. In these cases. because the slab is stronger than the lower mantle, the resistance to flow is only felt by the leading edge of the slab and is not transmitted up through the slab. None of these models are able to fit the observations that some (e.g., Tonga-Kermadec and Izu-Bonin) slabs may be in down-dip compression throughout.

Along the top surface of the subducting lithosphere within the subduction zone, the stress orientations rotate from horizontal extension approaching the subduction zone to horizontal compression. The steep dip of the fault (see Section 4.5.4) causes flow within the subducting lithosphere to change from a horizontal flow direction to flow at 30° parallel to the dip of the fault in the upper 10 km. This rapid change

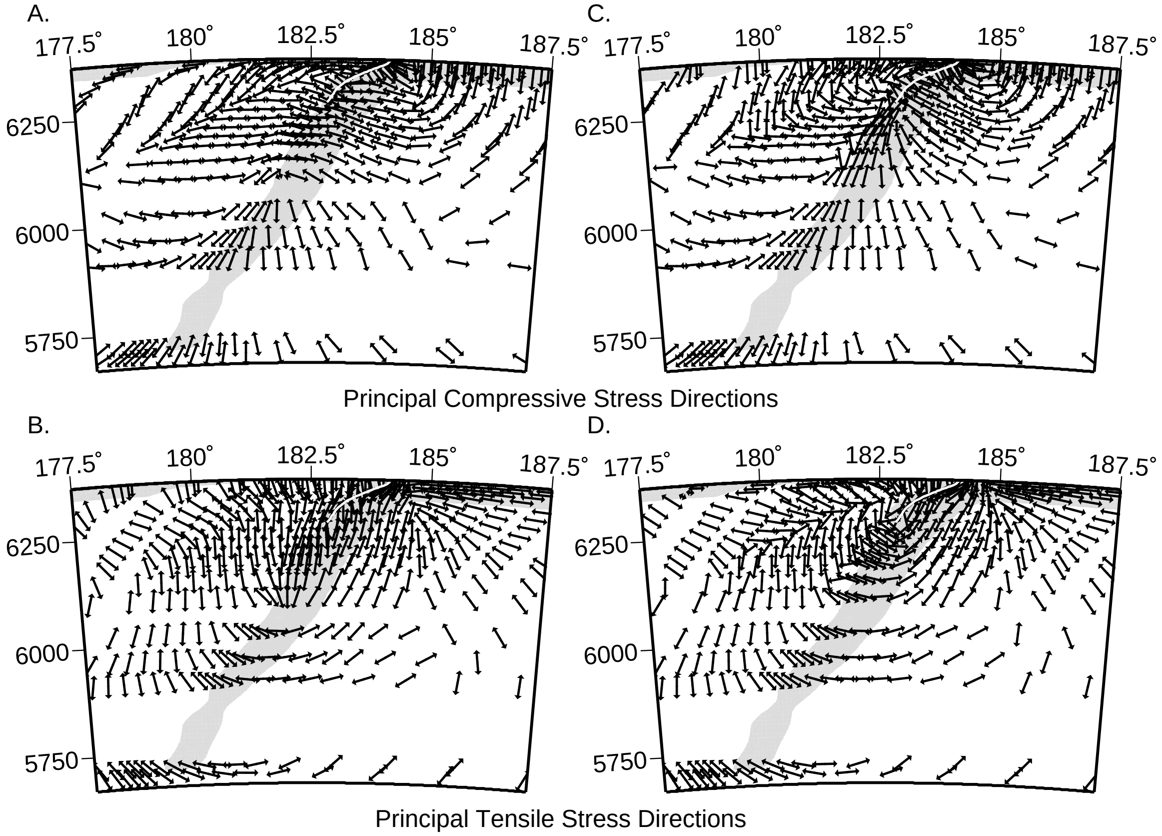

Figure 4.8: Principal stress directions. **A.** and **B.** are the principal compressive and tensile stress direction, respectively, for model 4byl. The slab is in down-dip tension from 100–350 km and down-dip compression below 350 km. **C.** and **D.** the same as **A.** and **B.** for model 4byl with a low viscosity wedge (fw9). The slab is in down-dip compression from the base of the lithosphere to 670 km.

in flow near the fault creates a small region of compression in the subducting plate seaward of the fault. These stress orientations are inconsistent with observations of extensive normal faulting of the subducting lithosphere within the trench [Chapter 2], indicating that this region is in horizontal extension throughout [Ogawa et al., 1997; Lee and Powell, 1982].

Young Lithosphere. In the models discussed above, the lithosphere on the overriding and subducting plates is assumed to be of uniform thickness determined by the age (50 Ma) of the plate. However, for some subduction zones, the upper plate contains a back arc spreading center with young lithosphere immediately above the slab. One example is the Tonga-Kermadec slab, which is overlain by the Lau and Havre trough spreading centers with lithosphere less than 5 Ma. Younger lithosphere translates into a thinner strong, dense boundary layer above the slab and influences the basin topography above the slab in two ways. First, since the lithosphere is thinner, the topography is shallower due to isostatic compensation (by 1.5–2.5 km) (Figure 4.6A). Second, the flow and pressure distribution above the slab are modified (Figure 4.6B–D). Flow in the wedge has a slight upward component of velocity entering the shallow portion of the wedge beneath the younger lithosphere. The region of low pressure above the slab becomes more concentrated toward the fault and a region of higher pressure forms along the surface beneath most of the region with very young crust. These changes lead to a narrower and slightly deeper basin closer to the trench, with positive dynamic topography on the side of the basin furthest from the trench. In addition, a small forebulge develops in models that did not have a forebulge with uniform lithosphere age or the forebulge height increases due to increased bending of the lithosphere in response to less viscous coupling between the shallow (500–100 km) portion of the wedge and the slab.

4.5.2 Low Viscosity Wedge Models

Understanding the dependence of topography, velocity and strain-rate on radial- and temperature-dependent variations in viscosity in these basic 2-D models provides the background needed to investigate the role of strong lateral variations in viscosity due to processes other than temperature variations. As discussed earlier, several lines of evidence (seismological, rock mechanics, geochemistry) suggest that the viscosity of the wedge may be several orders of magnitude less than the surrounding asthenosphere and mantle lithosphere. Billen and Gurnis [in press] [Chapter 3] presented the first results showing that a low viscosity wedge could reduce the basin topography on the overriding plate, making it possible to better match observed topography and geoid. In the following section we expand upon that initial study by fully exploring low viscosity regions of different shapes and viscosity, in models with different radial- and temperature-dependent viscosity structures.

Geometry of the Wedge. As the distribution of low viscosity material in the wedge is not well constrained by seismological observations, we test several different shapes for this region. The geometry of the LVW described by four parameters (d_{min}, d_{max}, w_b, w_t) is illustrated in Figure 4.9. These four parameters describe two types

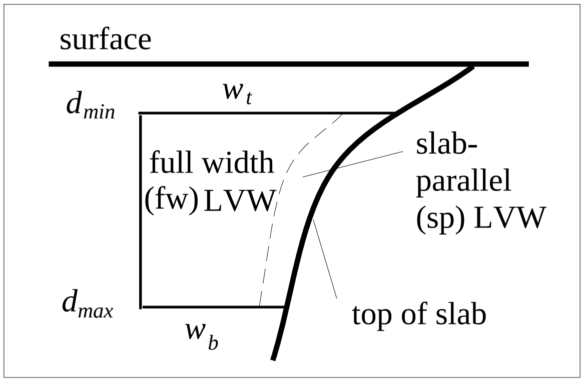

Figure 4.9: Geometry of the low viscosity wedge (LVW). d_{min} is the minimum depth to the top of LVW, d_{max} is the maximum depth to the bottom of LVW, w_b is the width of the base of LVW from the top of the slab, and w_t is the width of the top of LVW from the top of the slab.

of regions: full wedge (fw) for models with w_b and w_t greater than 100 km, and slab parallel (sp) for models with w_b and w_t less than 50 km (Figure 4.9). A full list of the 16 different wedge shapes tested are listed in Table 4.5.2. The influence of the LVW shape on topography of the overriding and subducting plate and distribution of flow in the wedge is first discussed for the background model 4byl. A subset of the wedge shapes is further investigated for background models 5byl and 6cyl.

Topography. Previous studies [Chapter 3] found that the influence of the LVW on basin topography depends strongly on the minimum depth of the LVW. For all 16 wedge shapes investigated, models with a minimum depth of 20 km reduce the basin depth by 6 km, while models with a minimum depth of 50 km only reduce the basin depth by 4 km. This is also true for the slab parallel LVW which extends only 50 km from the top of the slab. This result differs from previous results which found that a wide LVW was necessary to reduce the basin topography over the full width of the basin. However, these two results are consistent and the difference is due to the age of the overriding plate.

In previous models [Chapter 3] the overriding plate had a uniform age and therefore uniform thickness and density. In these models, a wide (200 km) and deep (200 km) low viscosity region was necessary to decrease the basin depth over the full width of the basin. If a narrower LVW was used, the basin depth was only reduced in

Table 4.5.2: 2-D Low Viscosity Wedge (LVW) Models

Model	d_{min}	d_{max}	w_b	w_t	h_{basin} (km)	Δh_{basin}	M
A-fw1	20	100	200	270	-2.35	5.81	98
A-fw2	20	100	100	170	-2.26	5.90	98
A-fw3	50	100	200	250	-3.74	4.42	97
A-fw4	50	100	100	150	-3.72	4.44	97
A-fw5	20	200	200	350	-2.35	5.81	97
A-fw6	20	200	100	250	-2.31	5.85	97
A-fw7	50	200	200	320	-3.51	4.65	97
A-fw8	50	200	100	220	-3.59	4.57	96
A-fw9	20	300	200	400	-2.36	5.80	97
A-fw10	20	300	100	300	-2.31	5.85	96
A-fw11	50	300	200	370	-3.58	4.58	95
A-fw12	50	300	100	270	-3.57	4.59	95
A-sp1	20	200	50	50	-1.94	6.22	96
A-sp2	20	200	50	50	-3.51	4.65	96
A-sp3	50	300	50	50	-1.95	6.21	96
A-sp4	50	300	50	50	-3.57	4.59	95
A-sz1a	0	120	40	40	-5.32	2.84	93
A-sz2a	0	120	40	40	-3.54	4.62	96
B-fw1	20	100	200	270	-5.39	6.20	89
B-fw5	20	200	200	350	-5.44	6.15	89
B-fw9	20	300	200	400	-4.94	6.65	90
B-sp1	20	200	50	50	-5.12	6.47	88
B-sz1a	0	120	40	40	-7.05	4.54	66
B-sz2a	0	120	40	40	-6.55	5.04	70
C-fw1	20	100	200	270	-6.54	14.24	97
C-fw5	20	200	200	350	-6.32	14.46	100
C-fw9	20	300	200	400	-6.30	14.48	100
C-sp1	20	200	50	50	-6.42	14.36	96
D-fw1	20	100	200	270	-5.33	6.26	90
D-fw5	20	200	200	350	-5.58	6.01	90
D-fw9	20	300	200	400	-5.43	6.16	90
D-sp1	20	200	50	50	-5.14	6.45	88
D-sz1b	0	120	40	40	-6.72	4.87	79
D-sz2b	0	120	40	40	-4.47	7.12	83
E-fw1	20	100	200	270	-5.59	6.00	88
E-fw5	20	200	200	350	-5.63	5.96	90
E-fw9	20	300	200	400	-5.43	6.16	90
E-sp1	20	200	50	50	-5.14	6.45	88
E-sz2c	0	120	40	40	-4.06	7.53	87

Geometry (d_{min}, d_{max}, w_t and w_b defined in Figure 4.9), basin depth, Δh_{basin} is the change in basin depth compared to model with no LVW, and M is mobility for models with a LVW for various background viscosity structures (see Table 4.5), and wedge viscosity. A: Viscosity Model 4byl, $\eta_{lvw} = 3\times10^{19}$ Pa s. B: Viscosity Model 5byl, $\eta_{lvw} = 3\times10^{19}$ Pa s. C: Viscosity Model 6cyl, $\eta_{lvw} = 3\times10^{19}$ Pa s. D: Viscosity Model 5byl, $\eta_{lvw} = 3\times10^{18}$ Pa s. E: Viscosity Model 5byl, $\eta_{lvw} = 3\times10^{17}$ Pa s.

the region above the LVW and increased beyond the LVW. As presented in the previous section, including young lithosphere on the overriding plate narrows the basin towards the trench and creates positive topography on the side of the basin furthest from the trench. The change in the geometry of the wedge caused by bringing lower viscosity asthenosphere into the shallow portion of the wedge beneath the young lithosphere has a similar affect as the LVW in the previous models. However, because the decrease in viscosity is only between the mantle lithosphere and the shallow portion of the wedge, the flow and pressure within the wedge is only modified slightly, and therefore the basin only becomes narrower, not shallower. Both young lithosphere and at least a narrow low viscosity region are necessary to eliminate the deep basin on the overriding plate.

The change in the shape of the low pressure region above the slab caused by introducing the LVW also increases the trench depth and leads to a forebulge on the subducting plate. The forebulge develops because the viscosity of the region above the slab decreases which reduces coupling of the slab buoyancy to the wedge causing higher stresses to be transmitted to the lithosphere.

As with the other viscosity parameters, it is important to determine whether the relative viscosity between the LVW and the slab or lithosphere influence the ability of the LVW to reduce the basin topography. For models without a LVW, the basin depth depends strongly on the slab viscosity. However, the LVW has the same effect on topography for models with a strong slab as it does for models with a weaker slab. Similarly, the topography is reduced by the same amount for models with $\eta_{lvw} = 3{\times}10^{19}$ Pa s as for models with $\eta_{lvw} = 3{\times}10^{17}$ Pa s (compare model sets B, D and E). Therefore, neither the relative viscosity between the slab and the LVW, or the lithosphere and LVW, controls the change in dynamic topography. Instead, the modification of the geometry due to the initial small change of the wedge viscosity has the largest effect on the topography.

Wedge Flow. While topography in models with a young lithosphere and LVW depends only on the minimum depth of the LVW and not the width or depth extent, the flow distribution in the wedge does depend on both the shape of the LVW and its viscosity. The shape of the wedge changes the shape of the pressure field above the slab. Instead of low pressure extending from the slab to the surface, the low pressure region is focused within the low viscosity region and a high pressure region forms above the LVW. However, the magnitude of the pressure above the slab is determined by the density anomaly and viscosity of the slab. Therefore, further reducing the viscosity of the LVW does not change the magnitude of the pressure. Instead the flow velocity increases since there is less viscous resistance and the same driving force transmitted to the wedge (see Appendix E).

In addition to higher velocities in the wedge, the LVW increases the plate mobility. For models 4byl, 5byl and 6cyl the plate mobility increases to ∼98 in the presence of LVW with $\eta_{lvw}/\eta_o = 0.1$. While the magnitude of velocity in the wedge continues to increase with decreasing wedge viscosity, only a modest increase in velocity of the slab occurs (1.5×) and is the same regardless of further decreasing the wedge viscosity.

Stress Orientations. As mentioned earlier, the Tonga-Kermadec slab (as well as sections along strike of other slabs) appears to be in down-dip compression at all depths. An important result of including a low viscosity region in the wedge is that the orientation principal stress axis in the shallow portion of the slab are oriented in down-dip compression along the top half of the slab (Figure 4.8C, D). This is the first time this aspect of the stress orientation within a slab has been reproduced in a fully dynamic model. The change in stress orientation within the slab is due to the change in coupling to the overlying wedge mantle. Without the LVW, the shallow portion of the slab is partially supported by viscous stresses from strong coupling of the wedge flow to the downward flow of the slab causing down-dip extension. This support of the slab from the material above is greater than the compressional stresses transmitted up through the slab, so the top portion of the slab is in extension while the lower portion of the slab is in compression. The LVW reduces the support of the slab from above, causing the shallow part of the slab to decouple from the larger scale flow and behave more as a viscous plate bending in response to the load of the slab beneath.

The orientation of principal stress directions in viscous bending (flexure) depends not on the curvature of the strong slab (as in elastic flexure), but on the direction in which the curvature is changing [Houseman and Gubbins, 1997]. For example, the compressional stress direction in viscous flexure aligns parallel to a surface becoming less convex (unbending) and perpendicular to a surface becoming more convex (bending). Therefore, it would be expected that as the surface of the lithosphere changes from strongly convex in the upper 100 km of the slab to less convex between 100 and 300 km, the orientation of the principal compressive stress axis would rotate from perpendicular to the slab surface to parallel to the slab surface. Therefore, the LVW decouples the slab from the overlying wedge allowing it to deform as a bending viscous plate independent from the flow in the wedge.

The LVW also modifies the orientation in stress within the overriding plate above the wedge. In models without a LVW the overriding plate is in horizontal compression, while models with a LVW are in horizontal extension in a region about 400 km wide beginning 150 km from the trench (Figure 4.8). Including a region of low density within the wedge broadens this region of extension, in particular for cases with a reversal of flow along the boundary of the LVW furthest from the slab.

4.5.3 Buoyancy in the LVW

If the low viscosity region within the wedge is due to melt or alteration of the mineralogy due to the presence of wate,r then it is likely that the LVW will also have a lower density than the surrounding mantle. Models with density anomalies of 10 and 20 kg/m^3 were investigated for four wedge geometries: fw1, fw5, fw9 and sp1 (Table 4.5.3). The smaller density anomaly leads to only a maximum 0.25 km increase in topography on the overriding plate for the largest LVW (fw9). The larger density anomaly leads to an increase in topography of up to 2.0 km, although the basin depth close to the trench only decreases slightly.

The positive buoyancy in the LVW has a strong influence on the flow in the wedge creating a large upward component of flow in the smaller, full width (fw1 and fw5) wedge models and a reversal of flow in the large (fw9) LVW with a 20 kg/m^3 density anomaly (Figure 4.10). A similar reversal of flow was found by Davies and Stevenson [1992] using kinematic models with superimposed flow of a small buoyant low viscosity region. They were able to achieve flow reversals with smaller buoyant regions due to much lower viscosity in the surrounding asthenosphere (3×10^{17} Pa s). They also

Table 4.5.3: 2-D Low Viscosity Wedge (LVW) Models with Positive Buoyancy

Model	**LVW Model**	$\delta\rho$ **(kg/m^3)**	h_{basin}	$\Delta h_{backarc}$	M
A-bw1a	fw1	10	-1.79	0.29	98
A-bw1b	fw1	20	-1.58	0.64	99
A-bw2a	fw5	10	-1.86	0.52	98
A-bw2b	fw5	20	-1.84	1.19	99
A-bw3a	fw9	10	-2.05	0.71	98
A-bw3b	fw9	20	-0.08	1.65	100
A-bw4a	sp1	10	-1.34	0.02	98
A-bw4b	sp1	20	-1.31	0.06	98
B-bw5a	fw1	10	-4.62	0.31	87
B-bw5b	fw1	20	-4.49	0.66	89
B-bw6a	fw5	10	-4.44	0.57	91
B-bw6b	fw5	20	-3.78	1.07	95
B-bw7a	fw9	10	-4.26	0.72	93
B-bw7b	fw9	20	-3.43	1.61	100
B-bw8a	sp1	10	-4.21	0.07	87
B-bw8b	sp1	20	-4.17	0.13	87

Basin depth, change in back arc height ($\Delta h_{backarc}$) and mobility (M) for models with a LVW and low density anomaly in the wedge for LVW's of various shapes (see Table 4.5.2) and background viscosity structure. A: Viscosity model 4byl, $\eta_{lvw} = 3\times10^{19}$ Pa s. B: Viscosity model 5byl, $\eta_{lvw} = 3\times10^{19}$ Pa s.

found that the reversal of flow depended on the integrated buoyancy, i.e., there is a trade-off between volume of buoyant material and the density anomaly. This explains why we only see flow reversal for the largest LVW and no noticeable change in flow for the slab parallel wedge.

4.5.4 Fault Singularity

The presence of the fault is required to create both asymmetric flow at the surface and trench morphology that resembles the observed morphology of trenches [Zhong and Gurnis, 1992, 1994; Zhong et al., 1998]. However, the fault also introduces a stress singularity into the model that leads to unconstrained trench depth on the subducting plate and fore arc height on the overriding plate. The magnitude of the stress singularity increases as the mesh size decreases. Therefore, in our models which have element sizes on the order of 2.5 km, much smaller than used in previous models [Zhong et al., 1998], this stress singularity leads to unreasonable trench depths and

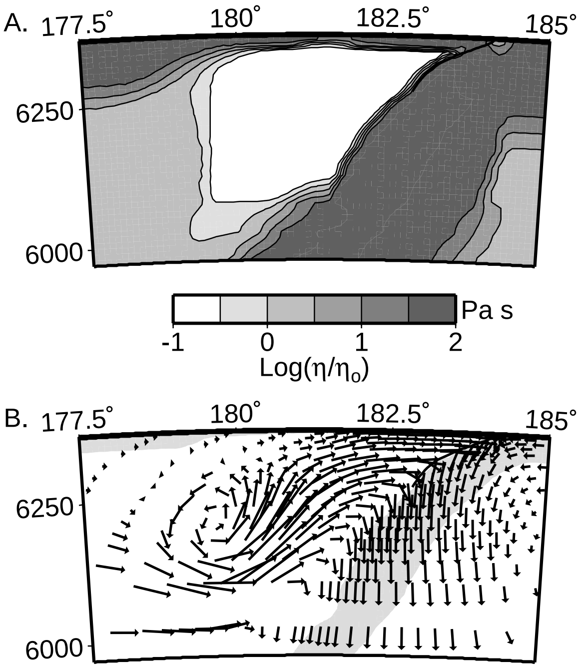

Figure 4.10: **A.** Viscosity model (contour interval is 0.5) and **B.** flow for model 4byl with a LVW including a density anomaly of -20 kg/m^3. A reversal of flow occurs near the boundary of the LVW furthest from the slab. The slab location is indicated by the shaded region ($T' < 0.5$)

fore arc heights. Another source contributing to the excessively deep trenches may be the dip of the fault used in our models. The fault dip at the surface for most subduction zones ranges from 10° to 20°. In our models a fault dip of less than 30° leads to numerical errors due to the distortion of the rectangular elements.

Stress at the fault can be constrained by reducing the viscosity around the fault, either by creating a weak zone surrounding the fault or using a yield stress. Physically this is justified because rock has finite strength, and if the stress is higher than this value, the rock yields limiting the maximum stress to the strength of the rock (elastic-plastic rheology) [Kohlstedt et al., 1995]. Both a yield stress and a narrow shear zone around the fault with a viscosity reduction of 0.1–1$\times\eta_o$ (for $\eta_{lith} = 100 \times \eta_o$ a yield stress of 75 MPa is used to focus the reduction in viscosity along the fault) decrease the trench topography to ~4–5 km and the fore arc high to less than 1 km. However, both of these methods lead to broadening of the trench by a factor of 2–3 where the deepest portion of the trench is shifted seaward up to 50 km from the fault tip and the trench profile of the subducting plate within the trench changes from convex to concave. This change in morphology is due to the width of the shear zone or yielded area, which usually includes 4–10 elements (8–22.5 km) on each side of the fault. This many elements is needed because the drop in viscosity across a single element must be less than a factor of 3 for numerical accuracy. Therefore, while the trench topography and fore arc high are greatly reduced, use of a yield stress or shear zone is not a satisfactory method for constraining the stress singularity at the fault.

4.5.5 Summary of 2-D Models

The large set of 2-D models explored illustrate the sensitivity of different observations to various aspects of the viscosity structure and provides constraints on the range and type of viscosity variations consistent with these observations. The main conclusions from these models areas follows:

1. The maximum viscosity of the slab is less than 3×10^{23} Pa s based on observations of strain-rates, stress orientations and plate mobility.

2. Weakening of the slab relative to the subduction zone lithosphere should be less than a factor of 100 for effective coupling of the lithospheric plate to the slab.

3. Including variations in lithospheric thickness due to plate age can modify flow in the wedge and dynamic topography if a young back arc spreading center is present above the slab.

4. A low viscosity region in the wedge greatly reduces basin topography on the overriding plate, changes the orientation of stress in the shallow portion of the slab from down-dip tension to down-dip compression and creates a region of horizontal extension in the overriding plate.

5. A large buoyant region in the wedge can cause a reversal of flow in the wedge, contributes to dynamic topography and broadens the region of extension on the overriding plate.

Based on these conclusions and results from previous modeling discussed in Section 4.2, we defined a preferred viscosity structure. This viscosity structure includes a strong lower mantle ($\eta_{lm}/\eta_o = 100$), a small increase in viscosity in the transition zone ($\eta_{tran}/\eta_o = 10$), a weak slab ($\eta_{slab}/\eta_o = 100$) with viscosity equal to the lithosphere viscosity ($\eta_{lith}/\eta_{slab} = 1$) and a low viscosity region in the wedge. None of the observations we used provide good constraints on the lithosphere or transition zone viscosity so these values are based on results from global geoid modeling. Our choice of equal slab and lithosphere viscosity is based on mobility constraints and probably only reflects what this ratio is within the subduction zone. The exact size, shape and minimum viscosity of the low viscosity region in the wedge are not constrained by these models.

4.6 3-D Models of the Tonga-Kermadec Subduction Zone

We begin our study of the 3-D dynamic flow in the Tonga-Kermadec subduction zone using the preferred viscosity structure described above excluding the low viscosity region (model 1). In addition to the constraints provided by topography, strain-rates and stress orientations, we now include the geoid as a further constraint on the 3-D viscosity structure. Although we know from the 2-D results that this basic model will not match observed topography, this model provides a reference as we add complexities to the viscosity and density structure. Eight 3-D models of the Tonga-Kermadec region are presented with cross sections of dynamic topography in Figure 4.11 and maps of dynamic topography and geoid in Figures 4.12 and 4.13. Table 4.6 lists each 3-D model with a description of the modifications to the viscosity or density structure. We also investigate the sensitivity of the predicted geoid to the deeper density structure of the slab using models that extend the slab density into the lower mantle (model 9) or along the 670 km discontinuity (model 10) (see Section 4.6.2).

The choice of radial- and temperature-dependent viscosity structure insures that the minimum strain-rate within the slab in our models is at least as large as the observed strain-rate release from seismicity and the minimum in strain-rate release occurs between 300 and 400 km depth (see Section 4.2.3). The orientation of stress within the slab for models with a low viscosity wedge (Models 3–10) is down-dip

Table 4.6: 3-D Models of the Tonga-Kermadec Subduction Zone

Model	**Viscosity Structure**	**Density Structure**
1	no LVW	Uniform thickness lithosphere
2	no LVW	Lithosphere thickness from plate ages
3	LVW, fw9	same as Model 2
4	same as 3	Add crustal density anomalies to Model 2
5	same as 3	Add low density in LVW, $\Delta\rho = 10$ kg/m^3 to Model 3
6	same as 3	Add low density in LVW, $\Delta\rho = 20$ kg/m^3 to Model 3
7	same as 3	Extend low density region 500 km west, $\Delta\rho =$ 20 kg/m^3
8	same as 3	Decrease slab density by factor of 2 and reduce crustal thickness of continent (see caption).
9	same as 3	same as 4 with slab thermal anomaly extended to 1000 km depth.
10	same as 3	same as 4 with slab thermal anomaly extended 1000 km to the west along the 670 km discontinuity.

Radial and temperature-dependent background viscosity structure is the preferred structure defined in Section 4.5.5 and is the same for all models ($\eta_{lm}/\eta_o = 100$, $\eta_{tran}/\eta_o = 10$, $\eta_{slab}/\eta_o = 100$, $\eta_{lith}/\eta_{slab} = 1$). Crustal density anomaly in models 3–7, 9, and 10 is 300 kg/m^3 with crustal thickness 9, 18 and 28 km for the Coleville ridge, Tonga-Tofua arc and continents. In Model 8, the thickness of the continental crust is reduced to 20 km to better match the observed topography.

compression along the top portion of the slab deeper than 300 km. However, between 100 and 200 km depth the principal compression axis are oriented 20–30° shallower than the dip of the slab. In addtion, while the principal compression axis are aligned perpendicular to the local strike of the slab (about 10°north of west), the principal tension axis include a component of along axis deformation. Therefore, the three-dimensional geometry of the slab affects the orientation of stress within the shallow portion of the slab. This result is not surprising given the along strike variation in the shape and depth extent of the slab and the conclusion from the 2-D models that including a LVW allows stresses due to viscous flexure within the slab to control the deformation of the slab. For 3-D models without a LVW, the stress pattern is the same as found in the 2-D models with some along axis compression in the shallow portion of the slab. The LVW in the 3-D models creates a more complex stress pattern within the shallow portion of the slab which more closely agrees with observations. Other changes to the 3-D models such as including low density regions in the crust or wedge have no visible affect on the stress orientation within the slab or overriding plate.

We begin by discussing the results for dynamic topography and the influence of dynamic topography on the predicted geoid (Section 4.6.1). The predicted geoid is then compared to the observed geoid (Section 4.6.2) using a spatio-spectral localization method [Simons, 1996]. This method enables us to compare geoid results from our regional models to the observed geoid without aliasing the long wavelengths due to truncation of the observed field spatially or spectrally. It is important to note that while slabs other than the Tonga-Kermadec slab are present within the region of the 3-D models, these slabs are not included in the models. Therefore, we focus our attention on the region within 1500 km of the Tonga-Kermadec Trench knowing that this will limit our ability to compare with observations at long wavelengths.

4.6.1 Dynamic Topography

The observed topography in the region of the Tonga-Kermadec subduction zone (Figure 4.2) is characterized by a narrow, deep trench and almost a 3 km difference in average depth between abyssal depths of the subducting Pacific plate (4–5 km) and shallow bathymetry (2–3 km) of the overriding Australian plate and back arc spreading system. Dynamic topography in models 1–3 display the same behavior described for the 2-D models. Model 1, with only radial and temperature dependent viscosity variations, has a broad (300 km), deep (6 km) basin on the overriding plate which clearly disagrees with the observed shallow bathymetry. In model 2, we include the

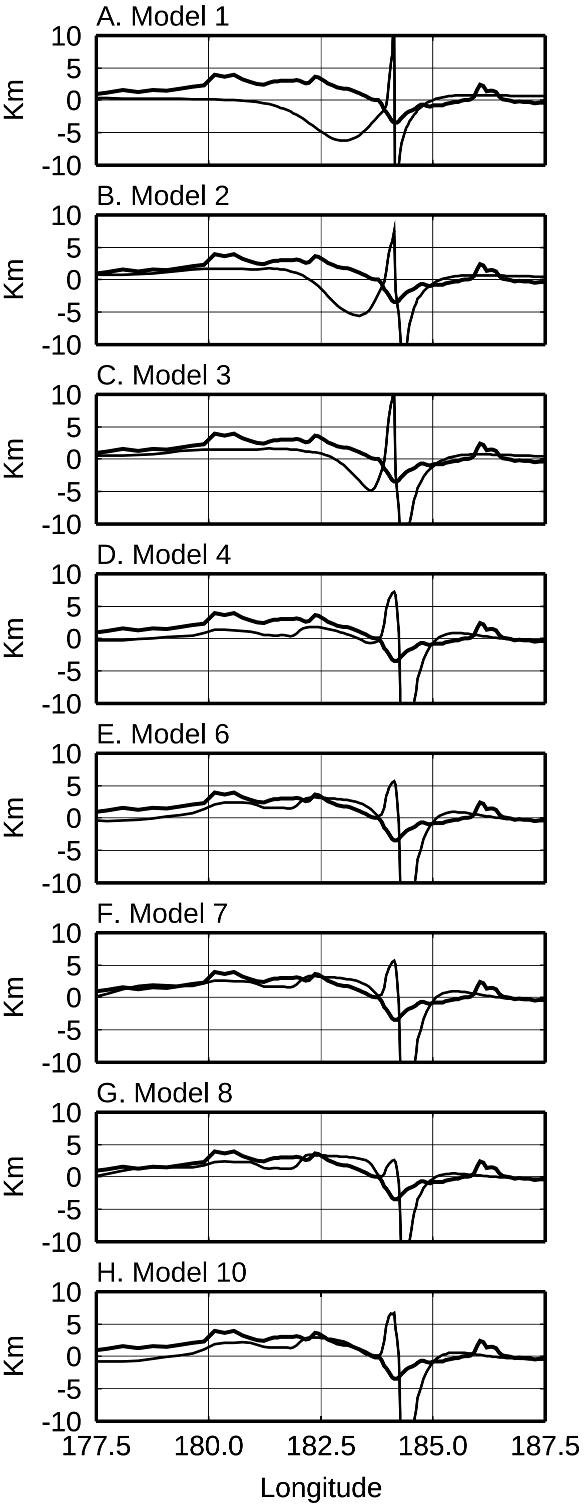

Figure 4.11: Cross sections of topography for 3-D models 1–4, 6–8, and 10 at 28°S. Observed topography (thick line) shifted up by 3.5 km for comparison with the predicted topography (thin line). Model parameters are listed in Table 4.6.

observed age variation of the lithosphere (see Section 4.4.2). Including these age variations narrows the basin but does not greatly improve the fit to observed bathymetry near the trench.

Model 3 includes a low viscosity region in the wedge along the entire length of the slab with dimensions perpendicular to the trench given by the 2-D low viscosity wedge shape, fw5 ($d_{min} = 20$ km, $d_{max} = 200$ km, $w_b = 200$ and $w_t = 350$ km). The basin is substantially reduced and the cross section (Figure 4.11C) shows that the long wavelength profile of topography across the trench is similar to the observed. However, the low region on the overriding plate is still 5 km deep. The basin on the overriding plate is completely eliminated in model 4 which includes crustal thickness variations due to the remnant and active island arc and continental crust to the southwest. Other crustal thickness variations exist within the model domain (mainly to the west of the south Fiji Basin), but are not included because they are far from the Tonga-Kermadec Trench. A narrow shear zone is included along the top surface of the fault. By limiting the shear zone to the overriding plate, we are able to decrease the height of the fore arc without increasing the width of the trench. Including the crustal anomalies and shear zone improves the agreement with the observed bathymetry at short wavelength. However, there is still a 1 to 1.5 km offset in the average depth on the overriding plate.

In the 2-D models decreasing the minimum viscosity of the wedge does not further decrease the basin depth. Therefore, in models 5 and 6 we include regions of low density material coincident with the LVW in an attempt to better match the average depth of the overriding plate. The density difference in model 5 is 10 kg/m^3 and in model 6 is 20 kg/m^3. The larger density anomaly in model 6 provides a good match to the average depth on the overriding plate in the region above the LVW (Figure 4.11E). However, the predicted topography decreases to the west while the observed topography remains shallow.

In model 7 we extend the low density region further west by 500 km. This improves agreement with the observed bathymetry and suggests that lower density material may exist in the shallow mantle throughout the region of past subduction extending to the New Caledonia basin [Kroenke, 1984]. Model 8 is identical to model 7 except

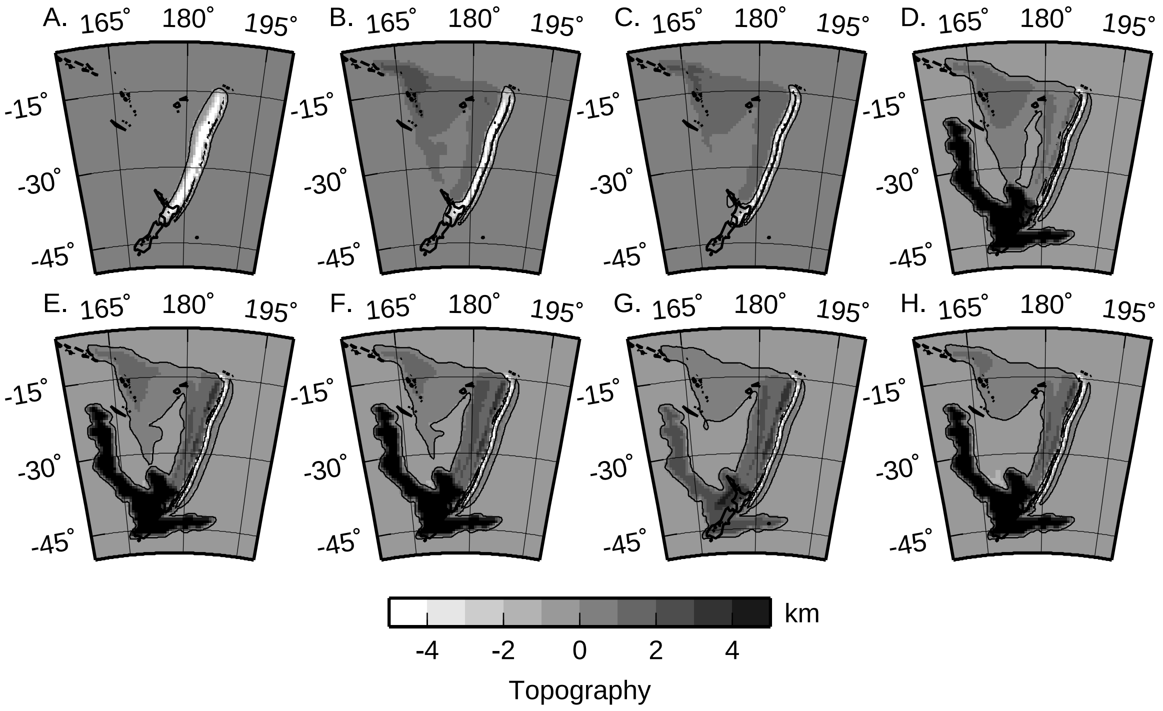

Figure 4.12: Maps of predicted topography for 3-D models. **A–D.** Models 1–4, **E–G.** Models 6–8, **H.** Model 10. See text for full discussion. Note that any variations in lithosphere age or crustal thickness within 300 km from the boundary domain are removed and set to an average background value for the ages (80 Ma) or zero for crustal thickness.

that the slab density is reduced by a factor of 2 (via a reduction in the coefficient of thermal expansion). Note that despite this large change in the driving force from the slab, the topography is only modified within 50 km of the trench. Similarly, in model 10, there is no change in the topography when the slab is extended along the upper-lower mantle boundary. These model will be discussed further with respect to how these changes in the density affect the fit to the geoid.

The importance of dynamic topography on the geoid is illustrated by the maps of predicted geoid in Figure 4.13. The deep basin in models 1–3 creates a broad (500 km) geoid low centered over the back arc region with an amplitude of 10 to 30 m. This geoid low narrows and shift towards the trench in model 3 (with a LVW). The long wavelength geoid is positive with an amplitude of 40 to 60 m. In models 4–10 the shallow density anomalies with the LVW creates positive dynamic topography that is not completely compensated by the density anomalies themselves. This leads to a much larger positive geoid at wavelengths of 500 to 1000 km with amplitudes

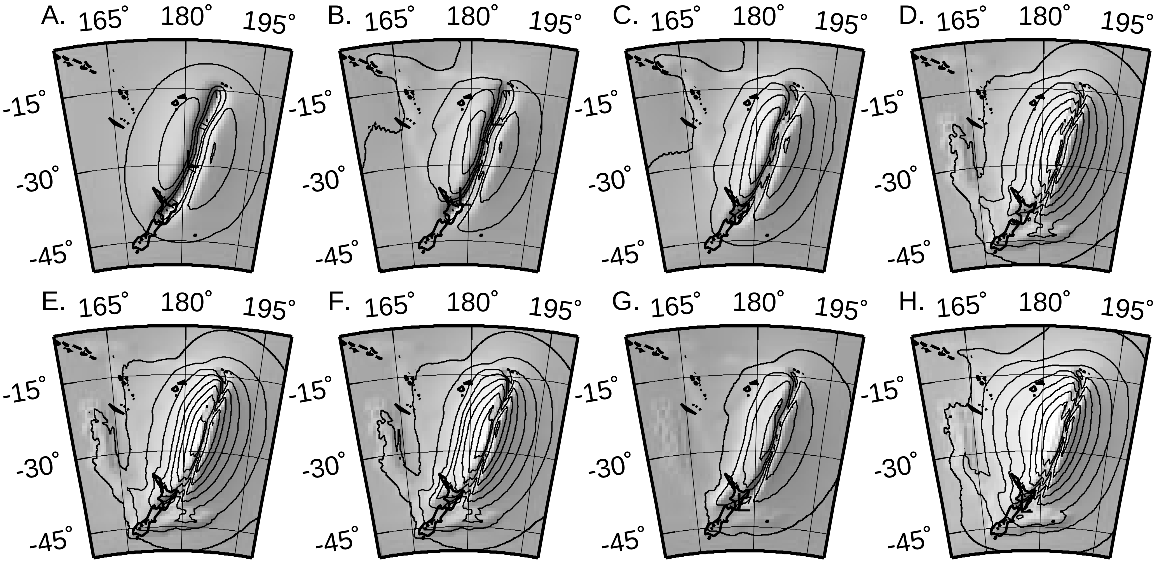

Figure 4.13: Maps of predicted geoid for 3-D models. **A–D.** Models 1–4, **E–G.** Models 6–8, **H.** Model 10. The predicted geoid is everywhere positive in these models. Local minimum are observed over the back arc region of trench depending on the model. Contour interval is 10 m. Note that because the fault singularity leads to unrealistically deep trenches, the maximum depth of the trench is limited to 5 km when calculating the geoid.

exceeding 100 m. In these models, the trench is marked by a small, short wavelength geoid low of 10–20 m.

In model 8, the amplitude of the medium wavelength geoid (500 km) is reduced by almost 40 m although the pattern remains the same as in model 7. The difference between the predicted geoid for models 7 and 8, which have almost identical topography, demonstrates the importance of using both the dynamic topography and geoid to constrain the viscosity and density distribution. The effect of the low viscosity region is to decouple the slab from the surface, rendering the topography insensitive to the buoyancy of the slab, while the geoid is still sensitive to both the driving force and the dynamic topography. We will return to this point in the discussion.

Finally, in model 10 extending the density anomaly of the slab west 1000 km within the transition zone increases the long wavelength geoid by 20–30 m over the north and south Fiji basins west of the trench, while above the trench the geoid only increase by 15 m. Since the predicted topography is not affected by these deeper density anomalies due to decoupling of the flow from the surface by the LVW, the amplitude of the geoid due to these deeper anomalies depends only on the magnitude

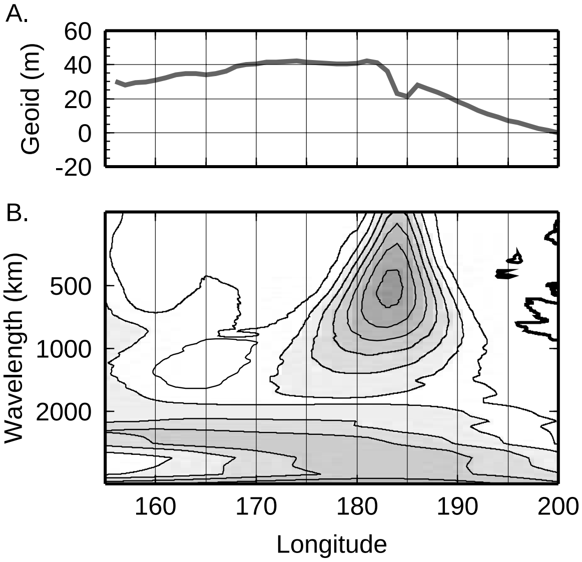

Figure 4.14: Localized R.M.S. amplitude for the observed geoid at 28°S. **A.** An east-west linear ramp is removed from the observed profile. **B.** Position and wavelength (harmonic degree) dependent R.M.S. amplitude of the observed geoid. Contour interval is 0.5.

of the density anomalies. Therefore, if the density of the slab in model 10 was also reduced by a factor of two as in model 8, we would expect the long wavelength geoid to decrease by a factor of two as well.

4.6.2 Multiscale Analysis of the Geoid

The observed geoid in Figure 4.1 over the Tonga-Kermadec region includes very long wavelength signal not included in our models. This makes it difficult to compare the results of our models to the observed geoid directly. Instead, we use a spatio-spectral localization method [Simons, 1996] to quantify the fit of the predicted geoid to the observed geoid as a function of position and wavelength. Simons [1996] showed that comparison between fields represented by a finite sum of spherical harmonics must take into account the spatial distribution of the source of the fields. If the sum is truncated, spurious signal may exist on regions of the sphere not spatially correlated with the source of the signal (Gibbs phenomena). The localized amplitude of the observed geoid is shown in Figure 4.14 as a function of position along an east-west profile at 28°S and wavelength. The R.M.S. amplitude reflects where the geoid has a large signal (power). In this cross section it is clear that the observed geoid has large signal at long wavelengths across the whole model domain, but only has large signal at short wavelengths in the vicinity of the Tonga-Kermadec Trench (185°) in this cross section.

The localization method developed by [Simons, 1996] is similar to wavelet analysis of time series where filtering at a given frequency is carried out within a moving time window where the window size is dependent on the frequency of interest. The filtering window in the spatial domain is a spherical cap with a characteristic spatial extent equal to twice the wavelength being considered. This choice of window balances the need for localization in both position and wavelength. Using this method we can calculate the localized R.M.S. amplitude of the observed and predicted geoid to assess what position and wavelengths make the largest contribution to the signal. In addition, we can quantify the fit of the predicted geoid to the observed by calculating the localized correlation and admittance between the two fields. While both the predicted and observed geoid are known up to degree and order 360 our analysis is limited to degrees between $L = 18$ and $L = 180$ (wavelengths of $\sim$100 to 100 km). The maximum and minimum harmonic degree is constrained by the size of the elements in our model and the size of the model domain. The maximum element size is about 1° (near the model boundaries) which corresponds to $L = 180$. The model domain extend 45° in longitude and latitude, corresponding to $L = 9$. However, because the boundary conditions affect the slope of the topography as it approaches the model boundary, we choose a more conservative minimum harmonic degree corresponding to half the size of the box. This is equivalent to limiting our analysis at long wavelengths to signals with a least two wavelengths across the domain.

The localization method provides three quantities to asses the success of a given model: correlation, R.M.S. amplitude and admittance. A good fit to the observed geoid would have high (> 0.8–0.9) positive correlations, non-zero R.M.S. amplitude and admittance equal to one over a large range of continuous positions and wavelengths. A high correlation where there is little power in the observed or predicted field is not considered significant. The correlation is sensitive to the position and structure of the fields, but not the amplitude. Admittance provides a measure of the ability of the dynamic model to predict the amplitude of the observed field: admittance greater than or less than 1.0 indicates that signal in the predicted field is too large or too small. Localized analysis of the predicted geoid for models 1, 3, 7 and 8 are presented in Figures 4.15–4.18 for cross sections through the 3-D models at 28°S (results do not vary significantly along the trench).

The misfit of the observed topography and influence of the dynamic topography on the geoid is reinforced in the position and wavelength correlations for model 1 (Figure 4.15). The offset of the geoid low towards the basin is seen in the high negative correlation from 180°–185° at short wavelengths (high harmonic degree, L = 100–180). While there are small local regions of high correlations, these are also regions of low amplitude in both the observed and predicted field and low admittance and therefore are not considered significant. At longer wavelengths (1000–2000 km, L = 36–18), the difference in the slope and lack of offset of the geoid at the trench is seen in the large negative correlation from 175°–200°.

The best fit to the geoid is found for model 3 (Figure 4.16) with a low viscosity zone but no crustal density anomalies or low density region within wedge. The localization finds large positive correlations (> 0.8) with the observed geoid at wavelengths of 250 to 1000 km (L = 160–36) over a 2000 km wide region across the trench. The R.M.S. amplitude is high throughout the region, while the admittance is greater than 1.0 indicating that while the pattern of the geoid is well matched, the amplitude is slightly too high. At the shortest wavelengths (< 250 km), the correlation decreases rapidly and the admittance increases beneath the geoid low over the trench. The trench and the narrow basin remaining on the overriding plate cause the geoid low to be broader and wider contributing to the misfit at the shortest wavelengths.

In order to match the observed topography, it was necessary to include sources of buoyancy in the crust and wedge. These sources of buoyancy increase the amplitude of positive dynamic topography at both short wavelengths over crustal buoyancy sources and long wavelengths over wedge buoyancy sources. The predicted geoid for models 4–7 and 9–10 are similar with large amplitudes over the subduction zone (Figure 4.13D–G). The correlation for model 7 (Figure 4.17) has local regions of high positive correlation directly beneath the trench and to the east at the shortest

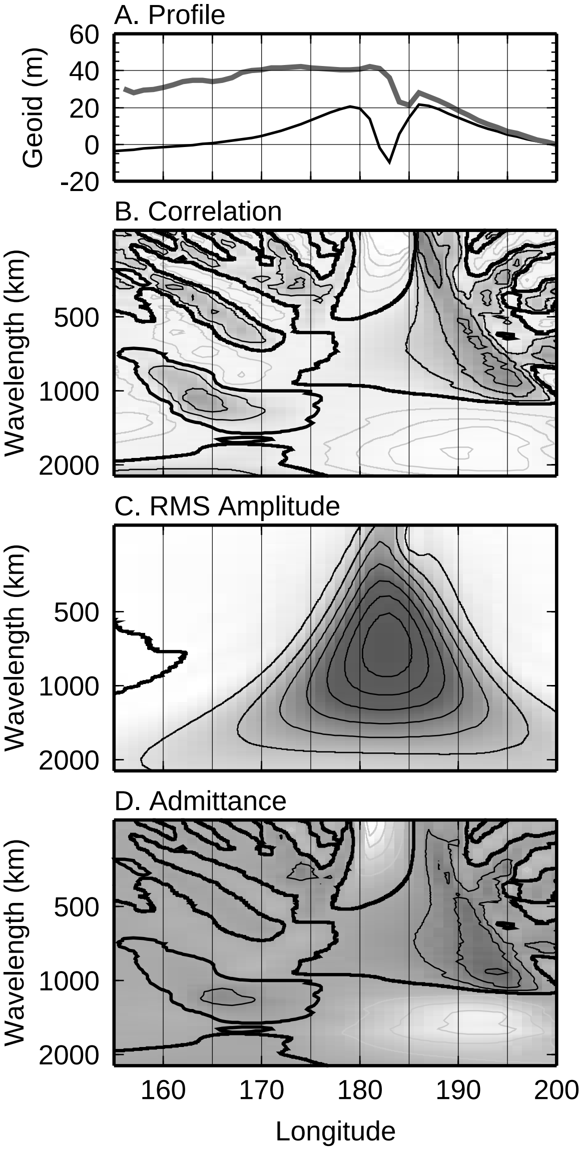

Figure 4.15: Geoid localization for model 1. **A.** Cross section of observed (thick line) and predicted (thin line) geoid at 28°S. An east-west linear ramp is removed from the profiles for comparison. **B.** Position and wavelength (harmonic degree) dependent correlation between observed and predicted geoid. Positive values are indicated by dark regions and black contours. Negative values are indicated by light regions and gray contours. Zero contour is marked by the thick black contour. Contour interval is 0.2. **C.** RMS amplitude of model geoid. Contour interval is 1. **D.** Admittance. Positive values are indicated by dark regions and black contours. Negative values are indicated by light regions and gray contours. Zero contour is marked by the thick black contour. Contour interval is 0.5.

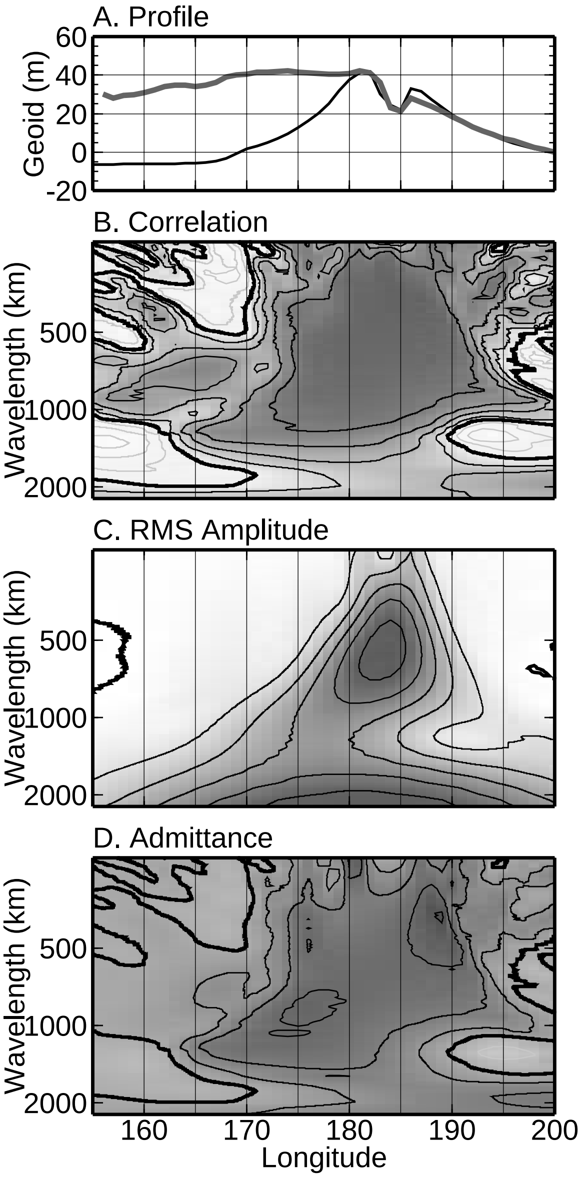

Figure 4.16: Geoid localization plots for Tonga model 3. Same as Figure 4.15.

wavelengths, and further west beneath the south Fiji basin and Lord Howe Rise. Including the density anomaly from the thick crust of the Lord Howe Rise improves the correlation with the geoid at wavelengths of 400–1000 km over this feature. However, the admittance for the Lord Howe Rise is high (>2.5) while the admittance for the high correlation regions close to the subduction zone are greater than 2.0, indicating that these features have much larger amplitudes than observed. This is clear over the trench where the predicted signal has a peak-to-peak amplitude of 60 m while the

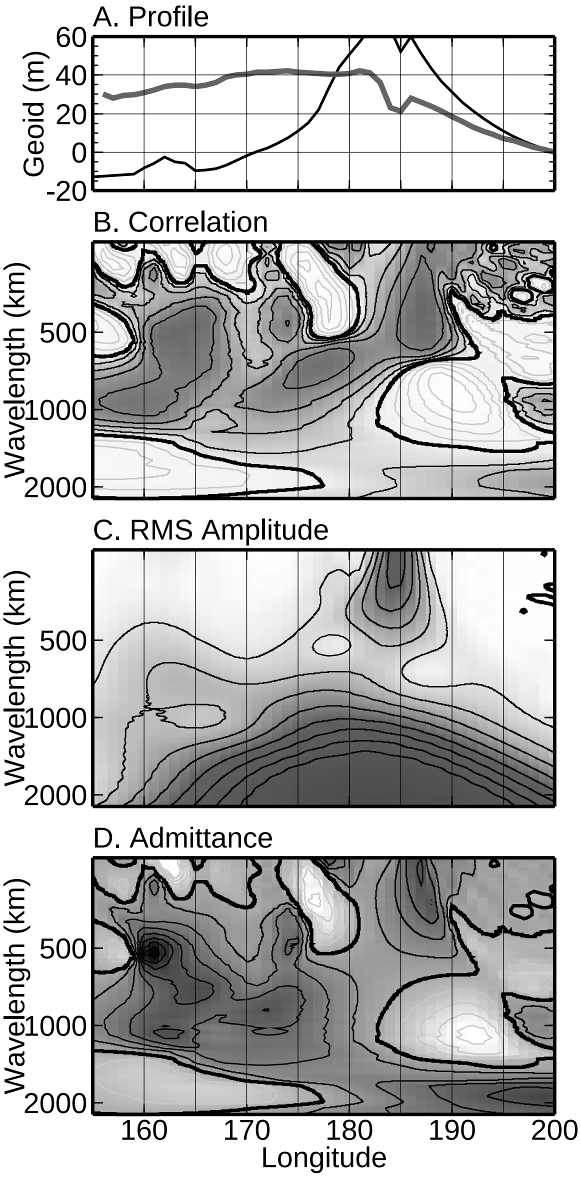

Figure 4.17: Geoid localization plots for Tonga model 7. Same as Figure 4.15.

observed is only 40 m. The local regions of negative correlation at wavelengths of 700–1000 km east of the trench indicate that not only is amplitude too large locally, the change in slope of the geoid approaching the subduction zone is also significantly different than observed.

The large difference between the predicted geoid in model 3 and model 7 is caused by the change in dynamic topography at the surface. Density anomalies very close to the surface are isostatically compensated by dynamic topography. That is, the contribution to the geoid from dynamic topography due to the density anomaly is the same magnitude and of opposite sign to the contribution due to the density anomaly itself, so these contributions cancel out and there is no net contribution to the geoid. However, as the density anomaly moves farther from the surface, its contribution to the geoid decreases, while the contribution due to dynamic topography depends on the viscosity structure. Even if the flow induced density anomaly is of the same magnitude as the density anomaly within the mantle, its contribution to the geoid will be greater because it is closer to the surface. In models 5–10, the low density region within wedge is not near the surface and therefore causes dynamic topography that is not exactly compensated for by this deeper low density anomaly. This leads to an overall increase in the amplitude of the geoid. Stated differently, in models 1–3 the large depression on the overriding plate caused by the flow from the slab partially compensates the positive geoid signal due to the slab density and this compensation decreases the geoid at short and long wavelengths.

The large amplitude of the geoid in model 7 indicates that either the positive dynamic topography predicted in these models is too high or the density of the slab is too large; these are the two positive contributions to the geoid. Since the predicted topography agrees well with the observed topography, this could be true if the low density region we have included in the wedge extends too deep. Alternatively, we could match the observed topography with a more shallow low density region with a larger density anomaly. The dynamic topography would then be more completely compensated by the low density region because it is closer to the surface, leading to less uncompensated positive dynamic topography. However, this change would have the largest effect over the back arc region, west of the trench, and would have less of an effect directly beneath the trench where the slab is closest to the surface and therefore has the largest affect on the geoid. Decreasing the density of the slab will also affect dynamic topography, but as seen in Figure 4.11, because the low viscosity region decouples the slab from the overriding plate, the main effect on topography is to decrease the trench depth and topography on the overriding plate within 50 km of the fault (in the fore arc).

The correlation with the observed geoid does improve when the slab density is

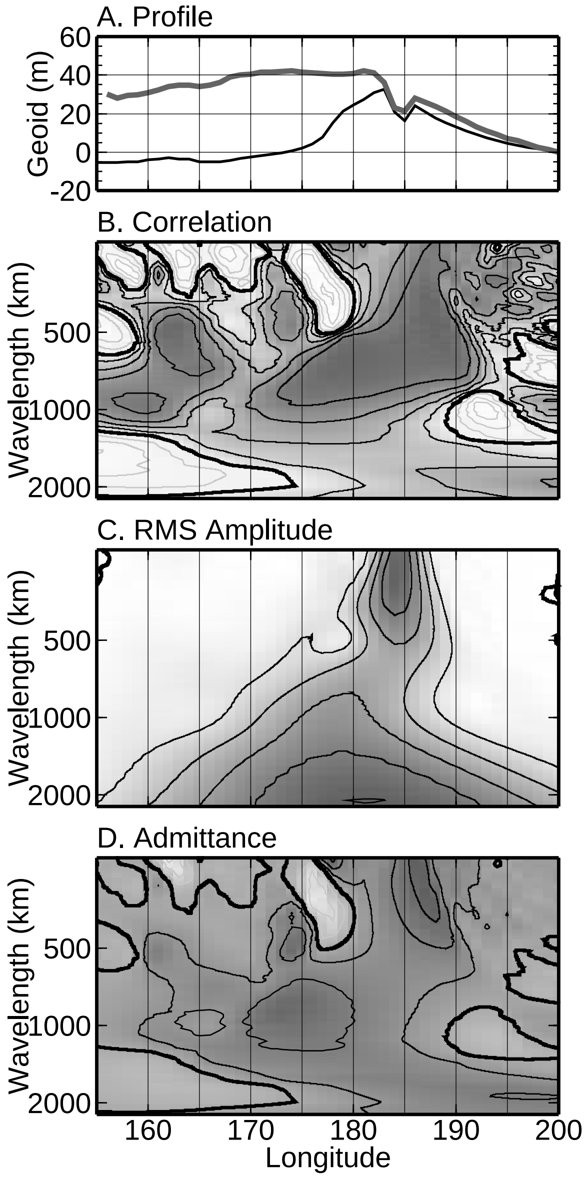

Figure 4.18: Geoid localization plots for Tonga model 8. Same as Figure 4.15.

decreased by a factor two (Model 8, Figure 4.18). The correlation over a 1000 km wide region beneath the subducting plate, trench and back arc region is greater than 0.8 at wavelengths ranging from 200 to 1000 km. The R.M.S. amplitude is high throughout these regions and the admittance is 0.75–1.5, with the highest values occurring at the shortest wavelengths beneath the trench. In addition, the thickness of the continental crustal anomalies are reduced in this model from 20 to 28 km in order to better match the observed topography over these regions. With this change the correlation across the Lord Howe Rise remains high, while the admittance is reduced to 0.8.

Although the agreement between the predicted and observed geoid is better in model 3 than in model 8, the constraint we have imposed to match both the topography and the geoid simultaneously leads us to conclude that model 8 is in fact a better model of the dynamics in the region of the Tonga-Kermadec Trench. The lack of agreement west of the back arc is in fact expected because there are other known sources of positive density anomalies (e.g., the New Hebrides slab) that are not included in this model. Other deeper positive anomalies may also be important as illustrated by the increase in the intermediate to long wavelength geoid (500–2000 km) in model 9 and 10. Tomography models of the Tonga-Kermadec region have a high velocity region extending west of the slab along the 670 km discontinuity [Zhao et al., 1997; van der Hilst, 1995]. There is some debate as to whether this seismic anomaly reflects a slab that is attached to the Tonga-Kermadec slab or is the remnant of Pacific Plate subduction to the south along the Vitiaz Trench [Brudzinski and Chen, 2000; Chen and Brudzinski, 2001].

4.7 Discussion and Conclusions

This study set out to investigate the influence of lateral variations in viscosity on several observations which could then be used to constrain the 3-D viscosity and buoyancy structure within the Tonga-Kermadec subduction zone and provide a self-consistent model of the dynamics over a broad range of length-scales. We have explored the influence of radial viscosity structure, slab viscosity, a low viscosity wedge and variable age lithosphere on the flow, stress field, dynamic topography and geoid. We find that by including density anomalies due to lithosphere age, crustal thickness and chemical changes within the wedge, we can model both the long and short wavelength topography. A fault included along the plate boundary is needed to form the trench and develop asymmetric subduction. However, numerical limitations prevent us from accurately modeling the depth of the trench or constraining the lateral viscosity structure within the trench or plate coupling along the fault. By limiting the trench depth to the observed depth (5 km) in calculating the geoid, we feel confident that the geoid results are robust at all but the very shortest wavelengths (less than 50 km) directly over the trench and that the conclusion that the slab density based on the thermal anomaly for the Tonga-Kermadec slab is too large is not likely to change when these numerical limitations are overcome.

Several aspects of the preferred viscosity structure derived from the 2-D models are consistent with previous modeling results (see Section 4.1): a moderate increase in viscosity from the upper to the lower mantle is necessary to match observation of down-dip stress orientation within the slab and to limit the height of the forebulge on the subducting plate to values consistent with observations (∼500 m). We have also shown how different aspects of the viscosity structure affect different observations and have placed stronger constraints on the range of viscosity values permitted. The magnitude of strain-rate provides a strong constraint on the absolute viscosity of the Tonga-Kermadec slab requiring that the viscosity be less than 3×10^{23} Pa s. The orientation of stress and coupling of flow between the slab and lithosphere require that the slab be weaker than the lower mantle, but not more than a factor of 100 weaker than the lithosphere within the subduction zone.

While several observations are easily explained by accounting for the strength of the slab and increase in viscosity from the upper to lower mantle, other observations require a low viscosity region in the wedge, a low density region in the wedge and/or a reduction in the inferred density of the slab. In particular we have found that several observations not before reproduced in a fully dynamic model are a natural consequence of including a low viscosity wedge (independent of temperature) within a radial- and temperature-dependent viscosity structure: down-dip compression within the shallow portion of the slab, extension of the overriding plate and positive dynamic topography on the overriding plate.

The change in stress orientation within the shallow portion of the slab from down-dip tension to down-dip or near down-dip compression when the wedge viscosity is decreased reflects a change in the mode of deformation within the slab. Two distinct modes of slab deformation characterized by differences in the flow and orientation of stress are observed. If the ratio of slab to wedge (or asthenosphere) viscosity is small, then the slab is strongly coupled to the larger scale flow within the subduction zone. The orientation of stress within the slab indicates that the slab flows into the mantle as a dense viscous body falling under its own weight. However, if the slab viscosity is increased or a low viscosity wedge is included, then the orientation of stress and pattern of flow are consistent with viscous flexure: the slab bends more than flows in response to the load of the deeper portion of the slab, independent of the surrounding flow.

Horizontal extension and a decrease in the basin size on the overriding plate can be understood as a consequence of decoupling the downward flow of the slab from the surface. Compression of the overriding plate observed in models without a LVW is caused more by the downward flow of the slab directly beneath the basin, and not by the horizontal flow of the lithosphere at the trench since this component of convergence is focused along the fault boundary.

In addition to providing a self-consistent explanation of geophysical observations within the Tonga-Kermadec subduction zone, a low viscosity region in the wedge is consistent with geochemical, petrologic and rock mechanics observations of other processes occurring within the wedge. In order to match the observed topography, it was necessary to include variations in lithosphere age, crustal thickness and a broad region of low density ($\Delta\rho = 20$ kg/m^3) material in the wedge. If the LVW is caused by water within the wedge from dehydration of the slab as we have proposed, then a lower density region within the wedge is consistent with the higher degrees of melting and depletion of the wedge material expected in presence of high concentrations of water. The fact that both of these changes are needed to match the geophysical observations strengthens our conclusion that the LVW is a self-consistent feature of the viscosity structure and an integral part of the subduction zone dynamics.

We found that in the 2-D models with young lithosphere above the wedge that the width of the low viscosity was not constrained. The need for a low density region several hundreds of kilometers from the slab indicates that the low viscosity region may also extend far from the slab. This result has important implications for the transport of fluids in the wedge and large scale flow above the slab. As shown for the 2-D model with a large low viscosity and low density region, a reversal of flow occurs at the edge of the low viscosity region. In the 3-D models this edge corresponds to the location of back arc spreading above the slab. It is not possible to know from our instantaneous models of flow whether this is coincidence or if a buoyant, low viscosity region is the result of or cause of back arc spreading. Previous attempts to explain back arc spreading have included difference in the absolute plate motion of the overriding plate and subducting plate such that the overriding plate had a net component of motion away the subducting plate [Chase, 1978] and the influence of trench rollback on the stress of the overriding plate [Scholz and Campos, 1995; Seno and Yamanaka, 1998]. While both of these mechanisms may take part in determining if the overriding plate is in extension, the LVW provides an additional local mechanism for back arc spreading consistent with explanations of slab rollback being caused by less coupling to the overriding plate and the observation that subduction zones with slabs in down-dip compression also have back arc spreading [Seno and Yamanaka, 1998].

The shallow bathymetry of the overriding plate in the Tonga-Kermadec subduction zone persists far from the active region of back arc spreading into region of previous island arcs and back arc spreading. By extending the region of low density material farther from the slab (500 km) we were able to match the observed shallow bathymetry. This suggests that as the trench shifts locations or retreats due to slab rollback, the regions of low density material created within the wedge may be left behind.

The effect of the low viscosity and low density region on dynamic topography has important implications for previous ideas about the compensation of density anomalies within the earth by density anomalies due to flow induced dynamic topography. Hager [1984] found that both a jump in viscosity and an increase in the density associated with slabs (by extending them beyond 670 km depth) was necessary to match the long wavelength geoid. Both of these conclusions were necessary to overcome the large negative contribution to the geoid from the dynamic topography above slabs. We find that lateral variations in viscosity modify the flow due to the slab and significantly decrease the amount of negative dynamic topography and the length-scales over which topography exists. If we also include shallow, low density anomalies in an effort to match the short to intermediate wavelength topography, then we find that the shallow density of the slab is too large, a very different result than found for the long wavelength geoid.

It is possible to match the shallow topography on the overriding plate with shallower density anomalies which would then contribute less to uncompensated dynamic topography. However, by decreasing the depth extent over which these density anomalies occur, the amplitude of the density anomalies would need to increase proportionally. The density anomalies needed to match the observed topography within a region extending to a depth of 200 km is 20 kg/m^3. Below 100 km depth this anomaly is attributed to reduction in the amount of garnet in highly depleted peridotite. Above 100 km, the anomaly is equivalent to having 4wt% in situ melt with a density of 2700 kg/m^3, a rather high in situ melt concentration to begin with. Therefore, limiting the depth over which this low density material exists to the most shallow parts of the mantle would require unreasonable melt concentrations to reach the needed decrease in density to match the topography. In addition, since this low density region may be needed to match the shallow bathymetry far west of the spreading center, it appears unlikely that high concentrations of melt within the crust could explain the shallow topography and that a deep region of low density is needed. Therefore, in our models the only way to match both the shallow topography on the overriding plate and the geoid is to decrease the density of the slab.

While our models do not constrain the exact depth range over which slab density must decrease, the localization results indicate that the shallow portion of the slab (0–250 km) directly beneath the trench and island arc needs to be less dense than predicted based on thermal anomalies. It is not clear what processes would lead to a lower density slab at this depth. It may be that the thermal anomaly of the slab in our models based on uniform viscosity asthenosphere is an overestimate. Indeed, the change in flow caused by a low viscosity wedge would likely lead to steeper temperature gradients along the top surface of the slab causing the slab to heat up more quickly. Another possible source of positive buoyancy in the slab is the depleted (residual harzburgite) layer at depths of 6 to 30 km beneath the basaltic crust. However, the positive buoyancy of this layer is offset by the negative buoyancy of the basaltic crust and there is no net positive buoyancy due to the composition of the slab [Ringwood, 1982].

Several of the results discussed have important implications for time-dependent processes within the subduction zone: back arc spreading, trench roll-back, and the thermal anomaly of the slab, which can not be fully addressed by instantaneous dynamic models. However, in using several different observations, the instantaneous models allow us to fully investigate the sensitivity of these observations to different aspects of the viscosity and buoyancy structure over a wide range of length-scales. In doing so we have found that subduction zone dynamics are strongly dependent on lateral variations in viscosity and that short wavelength structure can affect both the short and long wavelength dynamics. Finally, using several observations and a multiscale analysis of the geoid, we have found that the Tonga-Kermadec subduction zone probably has a low viscosity and low density region in the wedge and that the density of the slab may be smaller than predicted by simple thermal models. In the future, a similar multiscale approach applied to time-dependent models including a low viscosity wedge will be needed to explore the evolution of the wedge and slab thermal structure in a self-consistent dynamic model.

Appendix A Transformation of Citcom with Faults to Spherical Geometry

We developed **CitcomT** to solve viscous flow problems with faults in a spherical geometry. **CitcomT** is a transformed version of the 3-D Cartesian finite element code, **Citcom**, originally described by Moresi and Solomatov [1995], Moresi and Gurnis [1996] and Zhong et al. [1998]. Development of the Cartesian **Citcom** code of Zhong and Gurnis [1996] includes faults, a fully parallelized implementation and extensive benchmarking. So rather than create a completely new code with these same features in spherical geometry, we apply a coordinate system transformation to take advantage of these features in spherical coordinates. **CitcomT** gives identical results to **CitcomS** [Zhong et al., 2000], a more traditional finite element implementation of spherical flow without faults (see below).

For incompressible flow with an infinite Prandtl number and a Boussinesq approximation, the momentum and continuity equations are

$$\sigma_{ij,j} + \rho g \delta_{i3} = 0 \tag{A.1}$$

$$u_{i,i} = 0 \tag{A.2}$$

with summation over repeated indices. $\sigma_{ij,j}$ is the spatial derivative of the stress tensor, σ_{ij}, $u_{i,i}$ is the spatial derivative of the velocity vector u_i, and ρ and g are the density and gravitational acceleration. Equations (A.1) and (A.2) can be expressed in matrix form for each element within the computational domain [Hughes, 1987]:

$$KU + G^T P = F \tag{A.3}$$

$$GU = 0 \tag{A.4}$$

where K is the stiffness matrix which for the 3-D case with 8 nodes and trilinear shape function, has 24×24 entries, G^T and F are the divergence and force vectors, P is the pressure (constant within each element), $U \equiv (..., u_x^i, u_y^i, u_z^i, ...)$ is the velocity and $i = 1 - 8$ is the local node index.

The velocity in spherical coordinates U' is related to the velocity in Cartesian coordinates U by the transformation

$$U = RU' \tag{A.5}$$

where R is a 24×24 matrix with eight 3×3 sub-matrices along the diagonal for each local node given by

$$R_i = \begin{pmatrix} \cos\phi & \cos\theta\sin\phi & -\sin\theta\sin\phi \\ -\sin\phi & \cos\theta\cos\phi & -\sin\theta\cos\phi \\ 0 & \sin\theta & \cos\theta \end{pmatrix} \tag{A.6}$$

The momentum and continuity equations are transformed to spherical coordinates by substituting (A.5) into (A.3) and (A.4) and multiplying (A.3) by R^T:

$$K'U' + G'^T P = F' \tag{A.7}$$

$$G'U' = 0 \tag{A.8}$$

where $K' = R^T K R$, $G' = GR$ and $F' = R^T F$.

In practice the model is formulated in spherical coordinates. The transformation matrix for each node is formed and the mesh coordinates are then transformed to Cartesian coordinates. The matrices K, G^T and F are constructed in Cartesian coordinates. The transformation of K, G^T and F to spherical coordinates is applied and the equations are solved in spherical coordinates.

A.1 Faults in Spherical Coordinates

The matrix equations for faulted nodes in the Cartesian code are solved in a local coordinate system aligned with the fault surface [Zhong et al., 1998]. This change of coordinate system is also achieved by a transformation of Equations (A.3) and (A.4) from the global Cartesian coordinate system to a local coordinate system that differs for each faulted element. In this case the 24×24 entry transformation matrix Γ has only one nonzero sub-matrix, T:

$$T = \begin{pmatrix} n_1 & n_2 & n_3 \\ t_1 & t_2 & t_3 \\ s_1 & s_2 & s_3 \end{pmatrix} \tag{A.9}$$

where $\hat{n}$, $\hat{t}$ and $\hat{s}$ are the normal and tangential vectors to the fault plane.

To apply the transformation to spherical coordinates to faulted elements, we first apply the spherical transform R to the fault transform matrix Γ,

$$\Gamma_r = R\Gamma \tag{A.10}$$

Then, we apply the transformation from spherical to fault-oriented coordinates to Equations (A.7) and (A.8):

$$K'_f U'_f + G'^T_f P = F'_f \tag{A.11}$$

$$G'_f U'_f = 0 \tag{A.12}$$

where $K'_f = \Gamma_r^T K' \Gamma_r$, $G'_f = G' \Gamma_r$, $F'_f = \Gamma_r^T F'$ and U'_f is the velocity in the spherical-fault-oriented coordinate system. The velocity in spherical coordinates is given by $U' = \Gamma_r U'_f$.

Appendix B Dynamic Topography Benchmark

The geoid in a dynamic earth is the small difference between contributions due to internal density anomalies and density anomalies from dynamic topography on boundaries which requires accurate calculation of dynamic topography. Therefore, we need to verify that the topography calculation in **CitcomT** is capable of handling large variations in viscosity both radially and laterally. However, **CitcomT** is only capable of modeling part of a sphere, limiting the analytic solutions available to conduct these benchmarks. Specifically, analytic solutions exist for topography due to a harmonic load at depth with radial viscosity structure for a full sphere [Hager and O'Connell, 1981], but there is not a similiar solution for part of a sphere. Similarly, there exist analytic solutions for strong lateral variations in viscosity in Cartesian coordinates [Zhong, 1996], but not in spherical coordinates. Therefore, special consideration is needed to apply these types of benchmarks to the particular geometry and boundary conditions used in **CitcomT**.

B.1 Long Wavelength Topography and Radial Viscosity Structure

Since the spherical geometry of **CitcomT** is achieved due to a transformation of a Cartesian code (see Appendix A), the mesh boundaries follow lines of equal latitude and longitude within a region of a sphere. The side-walls of the region are subject to zero shear stress boundary conditions. These are *natural* reflecting boundary conditions in the east-west direction (e.g., a domain spanning 180° in longitude reflected once completes the sphere). However, in the north-south direction the rectangular elements become highly distorted near the pole as lines of equal longitude get closer together which could lead to errors in topography near the poles. In addition, these boundary conditions force the topography to have zero slope at the side-walls.

To test the topography calculation with radial viscosity variations, we would like to use the analytic results available for a full sphere [Hager and O'Connell, 1981]. These results use spherical harmonics to express lateral variations in the density and propogator techniques to solve for dynamic topography $h(\theta, \phi)$ at the top or bottom boundary:

$$\delta h^i_{lm} = \frac{1}{\Delta\rho_a} \int_c^a H^l(r)\delta\rho^i_{lm}(r)\partial r \tag{B.1}$$

and

$$h(\theta, \phi) = \sum_{lmi} \delta h^i_{lm} Y^i_{lm}(\lambda, \phi) \tag{B.2}$$

where l and m are the harmonic degree and order respectively, $\delta\rho^i_{lm}(r)$ are the harmonic coefficients for the density anomaly, δh^i_{lm} are the harmonic coefficients for the topography, $H^l(r)$ is the displacement kernel for the top ($r = a$) or bottom ($r = c$) surface, which depends on the radial viscosity structure, $Y^i_{lm}(\lambda, \phi)$ is the spherical harmonic and λ is colatitude.

The boundary conditions on the regional model preclude direct comparison to the analytic solution; therefore, we use an indirect method to benchmark the topography calculation. First, we compare topography from **CitcomS** [Zhong et al., 2000], a fully spherical finite element code, to the analytic solution for two-layer viscosity structures and a harmonic density anomaly at a single depth (0.25×a). Unlike **CitcomT**, **CitcomS** uses an equal area arrangement of elements that accounts for the pole and does not have side-walls. Second, we compare topography from **CitcomT** to topography from **CitcomSr**. **CitcomSr** is a regional finite element code otherwise identical to **CitcomS**. We use the same viscosity structures and density anomaly in a 45° × 45° region. The model topography in these two steps is calculated, using the standard pressure smoothing technique [Hughes, 1987], from the normal stress on the boundary ($h = \tau_{rr}/g\Delta\rho$). **CitcomT** is also able to calculate surface normal stress using the consistent boundary flux (CBF) method [Zhong et al., 1993]. This method has higher accuracy than the pressure smoothing technique especially when variations in rheology are present near the boundaries. Therefore, the final step is to compare topography from the pressure smoothing technique with topography from the CBF method for **CitcomT**. The results of this indirect test of the accuracy of the topography calculation are presented in Table B.1. This approach relies on the

Table B.1: Topography Benchmarks
for Radial Viscosity Variations

Model	r_{η_1}	$\frac{\eta_1}{\eta_2}$	$\delta h_t\%$	$\delta h_b\%$
1a	-	1	0.71	0.91
1b	0.75	100	0.65	1.34
1c	0.75	10000	0.67	1.12
1d	0.926	100	0.83	0.63
1e	0.926	10000	0.84	0.70
2a	-	1	0.09	0.27
2b	0.75	100	0.05	0.47
2c	0.75	10000	0.06	0.63
2d	0.926	100	0.11	0.26
2e	0.926	10000	0.10	0.26
3a	-	1	0.23	0.66
3b	0.75	100	0.28	0.60
3c	0.75	10000	0.27	0.55
3d	0.926	100	0.62	0.56
3e	0.926	10000	0.63	0.56
3f	0.9706	100	1.47	0.61
3g	0.9706	10000	1.52	0.60

Models used in the three-step benchmark of the long wavelength topography with a two layer radial viscosity structure. r_{η_1} is the radius of the boundary between the viscosity layers with values η_1 and η_2 for the top and bottom layers. $\delta h_t\%$ and $\delta h_b\%$ are the L_2-norm percentage errors for the top and bottom boundaries. 1a–1e compare **CitcomS** to the analytic solution for a $l = 4$, $m = 4$ harmonic density anomaly at a depth of 1600 km over a full sphere (resolution is 1°). 2a–2e compare **CitcomT** to **CitcomSr** for the same load over a 45°x45° region of a sphere (resolution is 1°). 3a–3g compare **CitcomT** results using the CBF and pressure smoothing technique.

initial benchmark of **CitcomS** to the analytic solution and the fact that **CitcomS** and **CitcomSr** are identical codes except for the boundary conditions.

Errors are less than 1% for all tests except the comparison of the CBF and standard pressure smoothing technique in **CitcomT** for the models with a large jump in viscosity two elements from the top surface (Models 3f and 3g). This error agrees with previous results for Cartesian models that demonstrate the CBF method is more accurate for models with viscosity variations near the boundaries [Zhong et al., 1993]. Although this three-step approach is not ideal, the consistently low errors at each step support our conclusion that the long wavelength topography, subject to the boundary conditions in the regional model, are accurately determined for models with strong ($10^4\times$) radial variations in viscosity.

Table B.2: Topography Benchmarks
for Lateral Viscosity Variations

Model	$\frac{\eta_1}{\eta_2}$	$\delta h_t\%$	$\delta h_b\%$
4a	1	0.037	0.11
4b	10	0.68	0.69
4c	100	0.80	0.81
4d	1000	0.82	0.82
4e	10000	0.82	0.82
4f	1×10^5	0.82	0.82
4g	1×10^6	0.81	0.82

Comparison of CitcomT topography with the analytic solution for a columnar viscosity structure. $\frac{\eta_1}{\eta_2}$ is the ratio of the viscosity in the two columns. η_1 is the viscosity for x = 0.05–0.1. $\delta h_t\%$ and $\delta h_b\%$ are the L_2-norm percentage errors for the top and bottom boundaries, respectively.

B.2 Short Wavelength Topography and Lateral Viscosity Structure

Strong lateral variations in viscosity may occur at plate boundaries due to variations in material properties and locally high stresses leading to short wavelength topography. To test the accuracy of the **CitcomT** finite element solution for models with strong lateral variations in viscosity, we use the exact analytic results for a columnar viscosity structure (a single jump in viscosity at the midpoint of the box) derived by [Zhong, 1996] for 2-D incompressible Stokes flow in a box with reflecting boundary conditions on the side-walls and free-slip boundary conditions on the top and bottom surface. The buoyancy is given by $\delta\rho(x', z') = -\sin(k_z z')\cos(k_x x)$ in a unit aspect ratio box. In spherical coordinates, x corresponds to longitude ϕ and z is depth.

In order to use these Cartesian solutions to benchmark **CitcomT** in spherical coordinates, we limit the width of the model domain to less than 0.1° on a 2-D transect at the equator. By limiting the size of the box, we insure that difference in lengths, volumes or areas due to the different coordinate systems are insignificant. Results are presented in Table B.2 for viscosity jumps up to 6 orders of magnitude.

Comparison of the analytic solution and model result for a 10^4 jump in viscosity is shown in Figure B.1. Errors are less than 1% for all the models demonstrating the accuracy of the **CitcomT** solution for short wavelength topography due to lateral

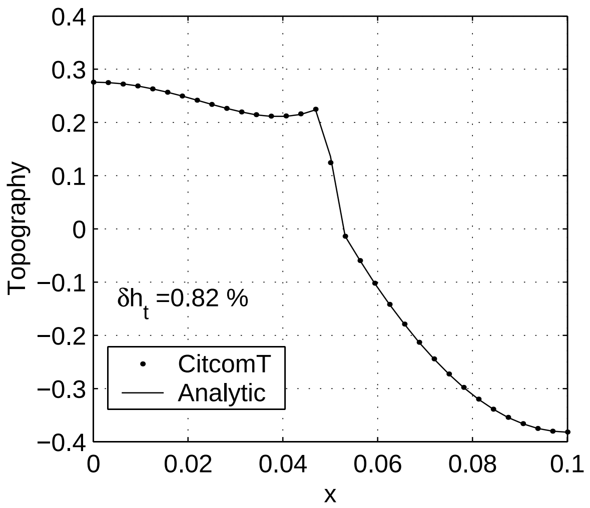

Figure B.1: Comparison of analytic and numerical topography for a columnar viscosity structure with a 10^4 jump in viscosity at the midpoint of the box.

variations in viscosity. These errors are consistent with extensive benchmarking by [Moresi et al., 1996] who argued that the viscosity should not vary by more than a factor of 3 across an element for errors to be less than 1%.

Appendix C Geoid and Gravity Calculation

To determine the geoid height and gravity anomaly of our models we solve directly for the harmonic coefficients of the anomalous potential due to density anomalies within the model domain and the resulting topography on the surface and core-mantle boundary.

The surface spherical harmonics, $Y^i_{lm}(\lambda,\phi)$, are a complete set of eigenfunction solutions to the angular dependence (colatitude λ and longitude ϕ) in LaPlace's equation. Therefore, any field which is function of λ and ϕ on a sphere can be represented as an infinite sum of spherical harmonics:

$$f(\lambda,\phi) = \sum_{lmi} f^i_{lm} Y^i_{lm}(\lambda,\phi) \tag{C.1}$$

where $\sum_{lmi}$ denotes the triple sum of $l = 0$–∞, $m = -l$–l and $i = 1$–2. The surface spherical harmonic, $Y^i_{lm}(\lambda,\phi)$, is defined as

$$Y^i_{lm}(\lambda,\phi) = P^m_l(cos(\lambda)) \begin{cases} \cos(m\phi), & i=1 \\ \sin(m\phi), & i=2 \end{cases} \tag{C.2}$$

where $P^m_l(cos(\lambda))$ are the normalized Associated Legendre Polynomials and l and m are the degree and order of the harmonic. Several normalizations of the Legendre polynomials are used; therefore, it is important to define these explicitly. We use a modified (by a pre-factor of $\sqrt{2l+1}$) Schmidt normalization:

$$P^m_l(cos(\lambda)) = \sqrt{2l+1} \times \begin{cases} P_{lm}(cos(\lambda)), & m=0 \\ \sqrt{2\frac{(l-m)!}{(l+m)!}} P_{lm}(cos(\lambda)), & m>0 \end{cases} \tag{C.3}$$

With this normalization the harmonic functions satisfy the following orthogonality condition:

$$\int_0^{2\pi}\int_0^{\pi} Y^i_{l'm'}(\lambda,\phi)Y^i_{lm}(\lambda,\phi)\cos(\lambda)\partial\lambda\partial\phi = \begin{cases} 4\pi, & l' = l \quad and \quad m' = m \\ 0, & l' \neq l \quad or \quad m' \neq m \end{cases} \tag{C.4}$$

C.1 Geoid and Gravity

The gravitational potential, V, is a solution of Poisson's equation for a given density distribution ρ:

$$\nabla^2 V = -4\pi\gamma\rho \tag{C.5}$$

where γ is the gravitational constant. Both the geoid height and gravity anomaly depend on the density anomalies in our model, i. e., the part of the density field that varies laterally. This includes the density anomaly associated with the topography on the surface and the core-mantle boundary. Therefore, we define the anomalous potential, δV due to the density anomalies $\delta\rho$ in our model. δV also satisfies Poisson's equation with $\delta\rho$ replacing ρ. The anomalous potential, outside a sphere with density anomaly distribution, $\delta\rho(r,\lambda,\phi)$, is given by

$$\delta V(Q) = \gamma \int_\Omega \frac{\delta\rho(r,\lambda,\phi)}{q} d\Omega \tag{C.6}$$

where q is the distance from the density anomaly at P (r,λ,ϕ) to the observation point Q (r_1,λ_1,ϕ_1) and $d\Omega = r^2\cos(\lambda)\partial\lambda\partial\phi\partial r$. Following Pollack [1973], the term $1/q$, the Green's function for Laplace's Equation in spherical coordinates, can be expressed in terms of spherical harmonics:

$$\tfrac{1}{q} = \textstyle\sum_{lmi} \tfrac{1}{2l+1} Y^i_{lm}(\lambda,\phi)Y^i_{lm}(\lambda_1,\phi_1) \begin{cases} r^l/r_1^{l+1}, & r_1 > r \\ r_1^l/r^{l+1}, & r_1 < r \end{cases} \tag{C.7}$$

For observations on the surface of the earth (radius R) and density anomalies in the interior, $r_1 > r$ and $r_1 = R$. Substituting Equation C.7 into Equation C.6, the coefficients for the geoid height due to density anomalies within the model domain,

$$N^i_{lm} = \int_\Omega \left(\frac{\gamma}{gR}\right)\frac{\delta\rho(r,\lambda,\phi)}{2l+1}\left(\frac{r}{R}\right)^l Y^i_{lm}(\lambda,\phi)d\Omega \tag{C.8}$$

and resulting topography on the surface and core-mantle boundary,

$$N^i_{lm}(h) = \int_S \left(\frac{\gamma}{gR}\right) \frac{h(\lambda,\phi)\Delta\rho}{2l+1} \left(\frac{r}{R}\right)^l Y^i_{lm}(\lambda,\phi) dS \tag{C.9}$$

The total geoid or gravity anomaly at a point on the surface (λ_1, ϕ_1) is then

$$N(R,\lambda_1,\phi_1) = \quad \textstyle\sum_{lmi} \left(N^i_{lm} + N^i_{lm}(h_t) + N^i_{lm}(h_b)\right) Y^i_{lm}(\lambda_1,\phi_1) \tag{C.10}$$

A similar expression for the gravity anomaly is found by substituting $(l+1)/r$ for $1/g$ in Equations C.8 and C.9.

C.2 Benchmarks

The calculation of the spherical harmonic coefficients described above is implemented as a post-processing step in the code **CitcomT**. Integration of the density anomalies within the domain and due to topography are carried out using finite element shape functions which have errors of less than 0.01%. The implementation and accuracy are verified by comparison with the analytic solution for the geoid anomaly due to a point mass, buried at a depth D in a sphere:

$$\partial N = \frac{\gamma M}{qg} \tag{C.11}$$

where $q = (t^2 + R^2 - 2Rt\cos(\alpha))^{1/2}$, $t = R - D$ and M is the mass. The geometry and comparison of the analytic and numerical results are presented in Figure C.1. The error is 0.04%.

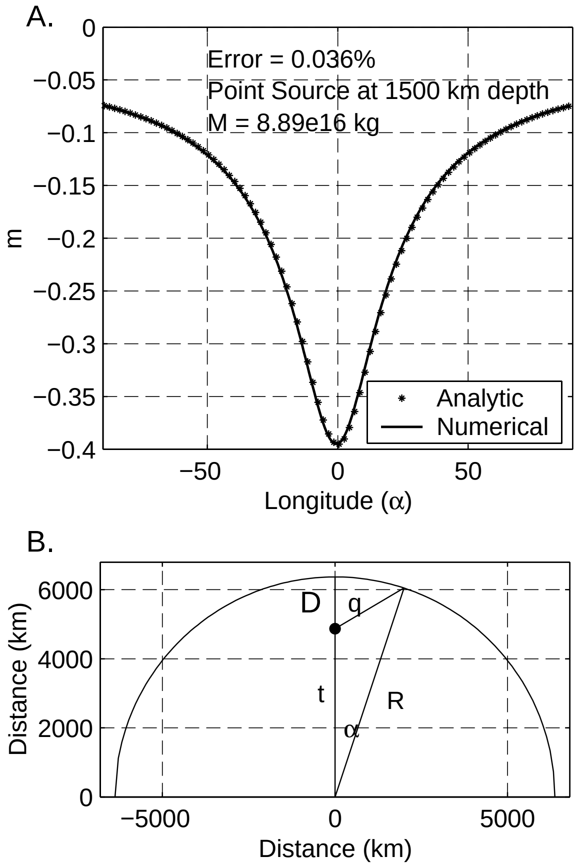

Figure C.1: **A.** Comparison of geoid anomaly for analytic (dots) and numerical (line) solution for a point source ($M = 8.89$ kg) buried at 1500 km depth in a sphere. The numerical solution includes harmonics through $l = 40$. The error is 0.036%. **B.** Geometry for the analytic solution.

Appendix D Slab Buoyancy

The buoyancy of the slab is due to the thermal structure of the slab. Ideally, we would like to derive the thermal structure of the slab starting with the temperature structure of the lithosphere and letting the temperature and flow evolve dynamically given a viscosity law. However, our understanding of the dynamics and the viscosity structure is not yet at the point where this kind model can be used to recreate the morphology of a particular slab. While the viscosity structure and time-dependence of subduction will influence the flow and the path the subducting slab takes to reach its present day position, the temperature of the slab will not depend greatly on the details of the path as diffusion will act to smooth the overall temperature distribution.

While the particular path of the slab has little effect on the final thermal structure, the boundary conditions and nature of the flow are important. Specifically, the thermal anomaly should be conserved: the total thermal anomaly of the slab and surrounding mantle must be equal to total thermal anomaly in the lithosphere before subduction. Models which assume isothermal boundary conditions on the surface of the slab [McKenzie, 1969] have a net loss of thermal anomaly leading to an underestimate of the slab buoyancy at depth.

We estimate the steady-state thermal structure of the slab using a kinematic model of the flow in the slab and surrounding mantle based on the analytic solution for viscous flow in a corner, known as corner flow. The standard corner flow solution [Batchelor, 1967] for viscous flow between two solid boundaries, one moving and one fixed, that meet at angle θ_0 depends on the the velocity U of the moving boundary, the angle θ_0 and the radial distance r from the corner:

$$\begin{aligned} u_r = &\quad A\cos\theta - B\sin\theta + C(\sin\theta + \theta\cos\theta) + D(\cos\theta - \theta\sin\theta) \\ u_\theta = &\quad -(A\sin\theta + B\cos\theta + C\theta\sin\theta + D\theta\cos\theta) \end{aligned} \tag{D.1}$$

where

$$A = \frac{U\theta_0}{(\theta_0+\sin\theta_0)} \quad C = \frac{2U\cos^2(\theta_0/2)}{(\theta_0+\sin\theta_0)} \quad D = \frac{-U\sin\theta_0}{(\theta_0+\sin\theta_0)} \tag{D.2}$$

and $B = 0$. The magnitude and distribution of the flow are completely determined by the geometry and U and do not depend on the viscosity of the fluid because the solid boundaries have infinite viscosity rendering the viscosity of the fluid, for any magnitude, small in comparison. This is of course different from flow in the mantle for which the viscosity of the slab may only be a few orders of magnitude greater than the surrounding mantle and the viscosity of the surrounding mantle may not be homogeneous. Nonetheless, the corner flow does simulate many features of the flow observed in dynamic models including the large scale corner flow above and below the slab and broadening of the flow and boundary layer above the slab with depth.

To estimate the thermal structure of the Tonga-Kermadec slab, the position of the top of the slab was determined from earthquake locations extending from the surface to approximately 670 km. Below the top surface of the slab, the flow is given by the corner flow solution with a dip angle, $\theta_0 \geq 90°$. The flow above the slab is given by the corner flow solution with a dip angle, $\theta_0 \leq 90°$, except for the top 100 km which is held fixed. Since the dip of the slab varies with depth, the flow at a given depth is determined using the local dip of the slab. The resulting field is not strictly divergence free, but the errors are small and do not affect the thermal structure. The velocity of the slab is fixed at an average rate of subduction based on plate reconstructions [Müller et al., 1993], approximately 5–10 cm/yr. The initial thermal structure of the lithosphere is defined as a half-space cooling profile for the age of subducting crust at the start of subduction. For Tonga the initial age of the subducting lithosphere is $\sim$50 Ma with some variation along strike of the trench [Chapter 1]. The thermal structure is then calculated from the advection-diffusion equation for the defined velocity field using the finite difference method until steady-state is reached, approximately 25 myr. The finite difference calculation is performed on a high resolution (5 km) mesh. The temperature field is then interpolated to the distorted finite element mesh. An example of the velocity field and thermal structure are given in Figure D.1.

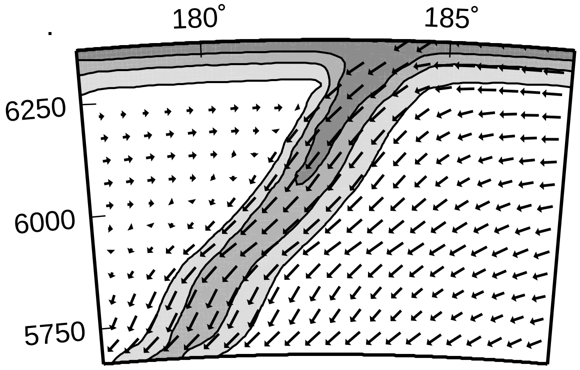

Figure D.1: Cross section of the corner flow velocity field used to calculate the input buoyancy field for the Tonga-Kermadec slab at 28°S. The flow consist of two corner flow solutions above and below the top surface of the slab with a maximum slab rate of 10 cm/yr. The steady-state temperature field results from $\sim$ 25 Myr of subduction. Contour interval is 400°C.

Appendix E Behavior of a Low Viscosity Region: 2-D Test Cases

To understand the effect of a spatially confined, low viscosity zone (LVZ) on topography and flow in the complex setting of a subduction zone, it is necessary to consider some simple geometries. We present results for three geometries in two dimensions that allow us to examine the influence of the relative position of the LVZ and a dense anomaly with radial and temperature-dependent variations in viscosity.

Figure E.1 illustrates the three geometries used. In all models the LVZ is in the same position, 50 km from surface 200 km wide and 150 km high. The position of the 2-D cylindrical density anomaly is shifted relative to the LVZ, placing it either next to the LVZ (position A, z = 150 km), below the LVZ under the right-hand corner (position B, z = 250 km) or centered under the LVZ (position C, z = 250 km). These three positions are used to understand how the relative position of the slab and a low viscosity region in the wedge will influence topography and flow. The viscosity of the LVZ is 100 times less than the surrounding asthenosphere (reference viscosity is

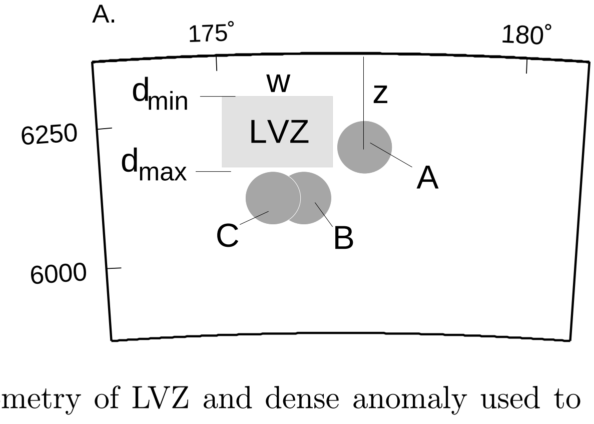

Figure E.1: **A.** Geometry of LVZ and dense anomaly used to investigate the effect of the LVZ on topography and flow. The LVZ position is fixed with d_{min} = 50 km, d_{max} = 200 km and w = 200 km. The dense anomaly can occupy three positions: A, next to the LVZ at z = 150 km; B, below the right corner of the LVZ at z = 250 km; C, centered below the LVZ at z = 250 km.

$3{\times}10^{20}$ Pa s used to dimensionalize topography and velocity). The density anomaly of the sphere is 50 kg/m^3. For each position of the density anomaly, we test four viscosity models:

1. Uniform viscosity, including the dense cylinder (except for the LVZ when it is present).
2. Strong cylinder, with the cylinder viscosity, $\eta_{cyl} = 20 \times \eta_o$.
3. Strong cylinder with strong lithosphere ($z = 100$ km), $\eta_{lith} = 100 \times \eta_o$.
4. Strong cylinder with strong lithosphere and lower mantle ($z > 700$ km), $\eta_{lm} = 100 \times \eta_o$.

For comparison we also calculate the flow and topography for each viscosity structure without the LVZ (Figure E.2). In these cases the cylinder is in position A. Topography profiles for the model without a LVZ are shown in Figure E.3A. As found by Koch and Ribe [1989], increasing the viscosity of the cylinder increases the amplitude of surface topography as does including a strong lithosphere. Both of these changes increase the coupling of flow above the cylinder. Adding a strong lower mantle decreases the surface topography inhibiting flow beneath the slab which decreases the amplitude of the low pressure region above the cylinder pulling down on the surface. In each of these models, the pressure and velocity field are symmetric across the center of the cylinder.

The pressure and flow field for each back ground viscosity model including a low viscosity zone are shown in Figures E.4–E.6 for the three different positions of the dense cylinder. For models with the dense cylinder next to the LVZ, the main effect of the low viscosity region is to decrease topography above the LVZ and increase the depth of the basin above the cylinder (Figure E.3B). The pressure and velocity remain fairly symmtric for cases without a strong lithosphere or lower mantle (Figure E.4A, B). For the case with a strong lower mantle and lithosphere, flow is trapped in upper mantle and focuses in to local cell strong flow within the LVZ (Figure E.4D).

The LVZ has a much stronger influence on topography and flow for cases in which the LVZ is above the dense cylinder (Figures E.3C, B and E.5–E.6).

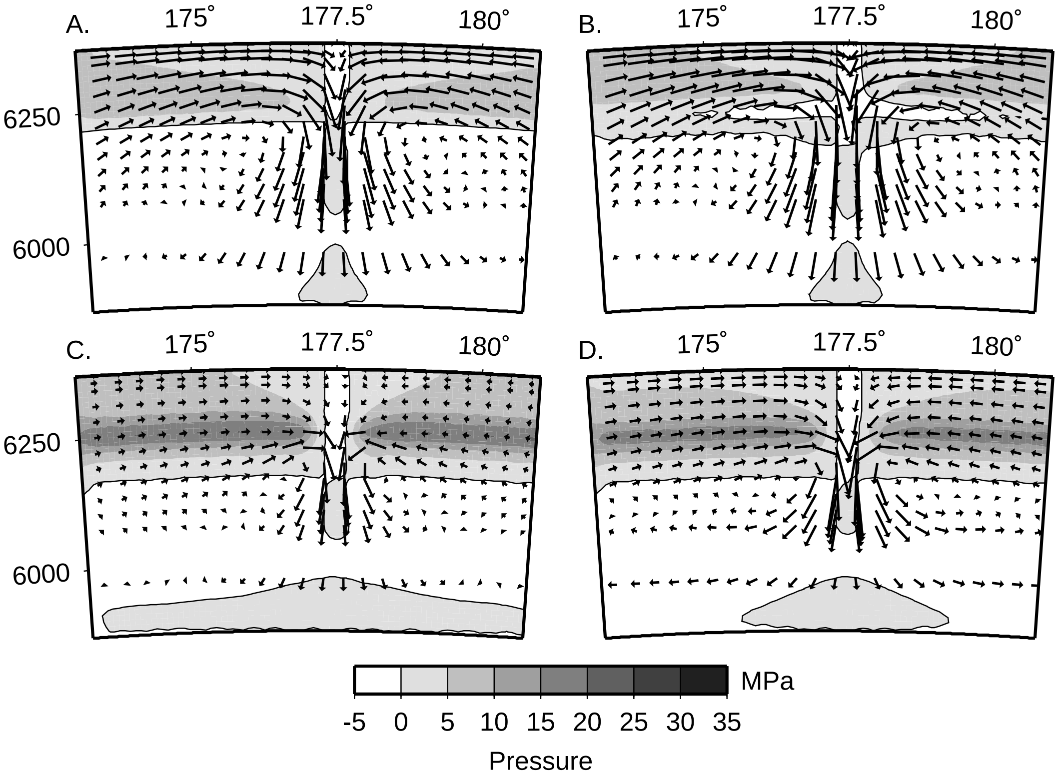

Figure E.2: Pressure and flow for models with uniform background viscosity including the cylinder. Velocities are scaled by the maximum velocity in each model. **A.** Uniform viscosity, except for LVZ (v = 4.3 cm/yr). **B.** Strong cylinder (v = 3.2 cm/yr). **C.** Strong cylinder and lithosphere (v = 0.4 cm/yr). **D.** Strong cylinder, lithosphere and lower mantle (v = 0.2 cm/yr).

In these models, the deep basin above the dense cylinder is almost completely eliminated. Instead a broad region of low topography (less than 0.2 to 0.4 km) forms above the LVZ deepening above the cylinder in Position B (below the corner of the LVZ). In each model including a LVZ we find that the relative amplitude of topography found in the models without a LVZ remains the same: amplitude of topography is largest for the case with a strong cylinder, lithosphere and lower mantle. We also find that for cases with a strong lithosphere, the sharp decrease in viscosity at the corners of the LVZ within the lithosphere create sharp horizontal gradients in pressure which lead to short wavelength topographic highs within the broader low.

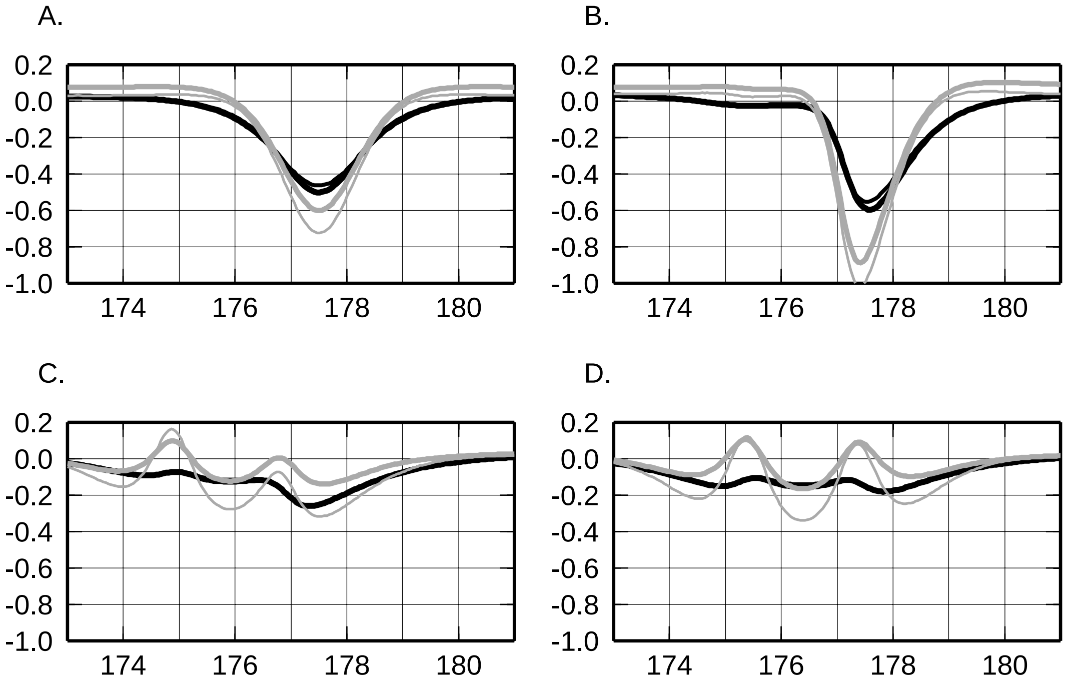

Figure E.3: Topography profiles for each of the background viscosity models Model 1, thin black; Model 2, thick black; Model 3, thin gray; Model 4, thick gray. **A.** No LVZ. Dense cylinder is in position A. **B.** Strong cylinder. **C.** Strong cylinder and lithosphere. **D.** Strong cylinder, lithosphere and lower mantle.

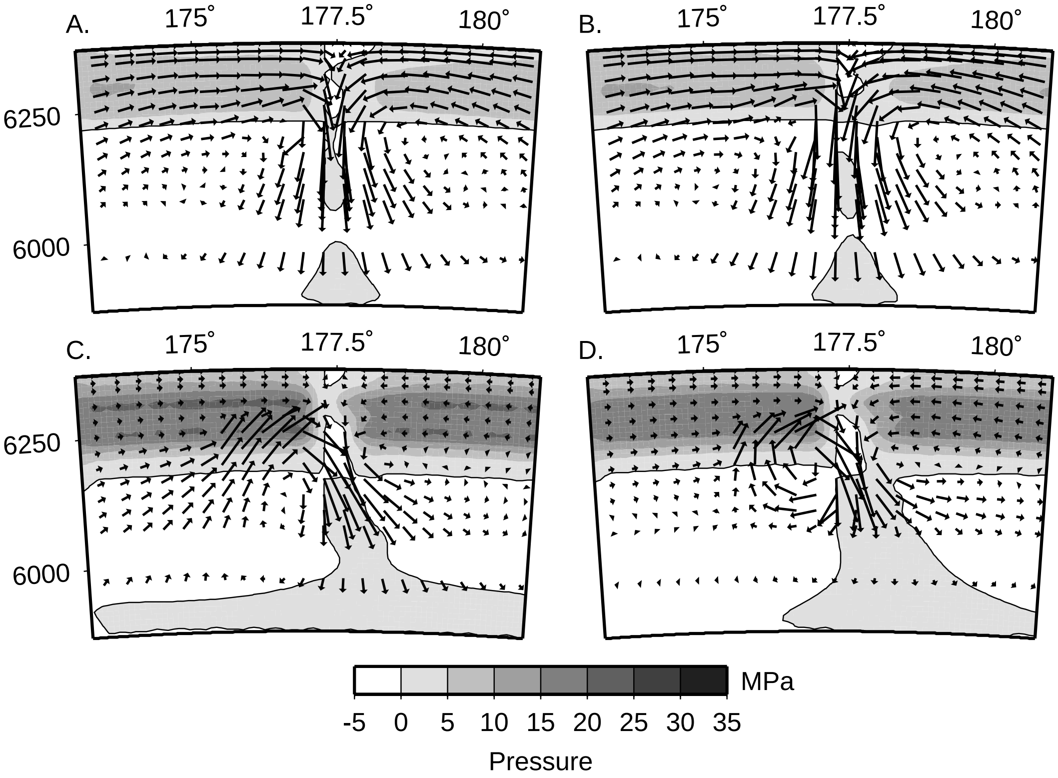

Figure E.4: Pressure and flow for models type 1–4 with cylinder in position A. Velocities are scaled by the maximum velocity in each model. **A.** Uniform viscosity, except for LVZ (v = 5.3 cm/yr). **B.** Strong cylinder (v = 3.9 cm/yr). **C.** Strong cylinder and lithosphere (v = 0.4 cm/yr). **D.** Strong cylinder, lithosphere and lower mantle C (v = 0.3 cm/yr).

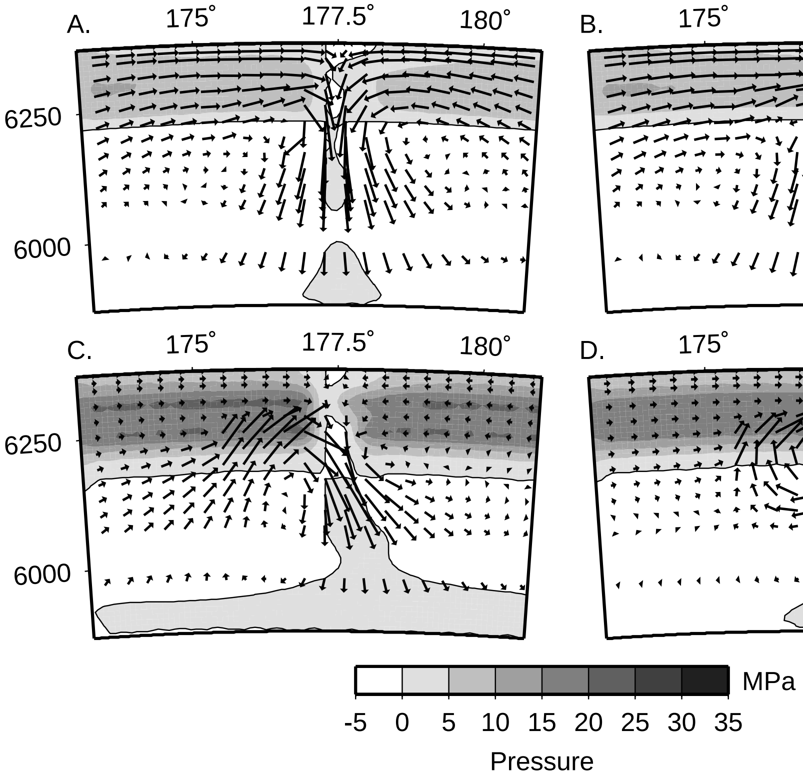

Figure E.5: Pressure and flow for model types 1–4 with cylinder in position B. Velocities are scaled by the maximum velocity in each model. **A.** Uniform viscosity, except for LVZ ($v = 8.1$ cm/yr). **B.** Strong cylinder ($v = 5.7$ cm/yr). **C.** Strong cylinder and lithosphere ($v = 2.9$ cm/yr). **D.** Strong cylinder, lithosphere and lower mantle ($v = 0.8$ cm/yr).

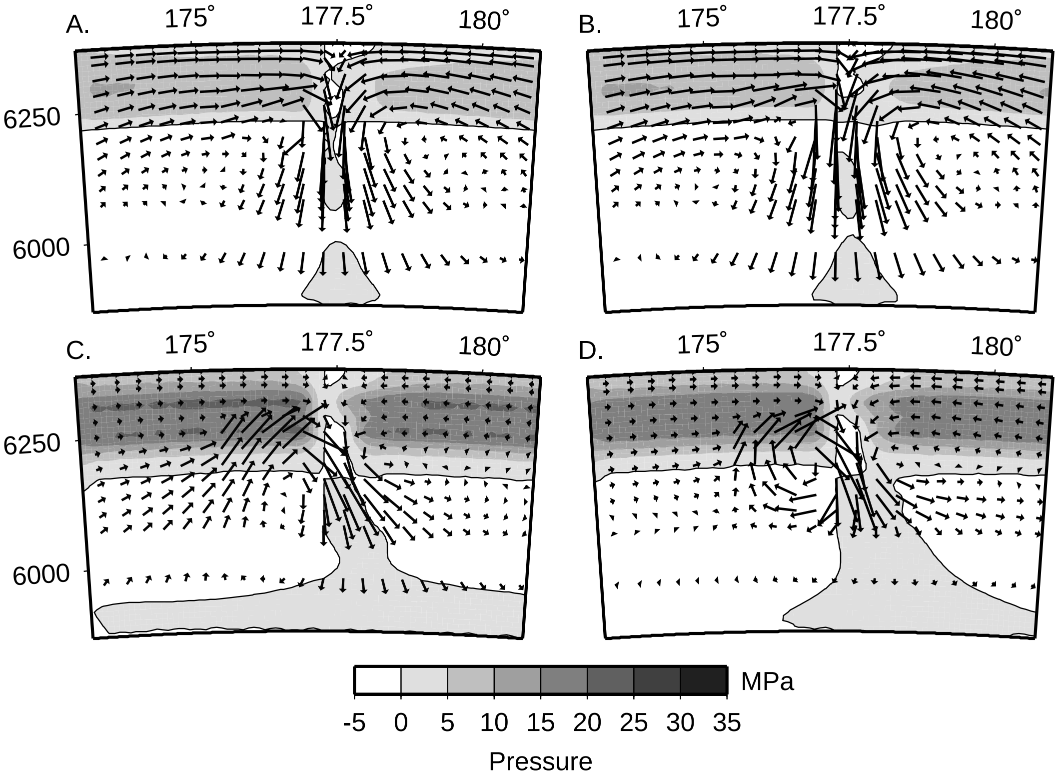

Figure E.6: Pressure and flow for models types 1–4 with cylinder in position C. Velocities are scaled by the maximum velocity in each model. **A.** Uniform viscosity, except for LVZ (v = 8.6 cm/yr). **B.** Strong cylinder (v = 6.1 cm/yr). **C.** Strong cylinder and lithosphere (v = 2.9 cm/yr). **D.** Strong cylinder, lithosphere and lower mantle (v = 0.8 cm/yr).

References

K. Denise Apperson and Cliff Frohlich. The relationship between Wadati-Benioff Zone geometry and P, T and B axes of intermediate and deep focus earthquakes. *Journal of Geophysical Research*, 92:13821–13831, 1987.

M. Barazangi and B. Isacks. Lateral variations of seismic-wave attenuation in the upper mantle above the inclined earthquake zone of the Tonga Island Arc: deep anomaly in the upper mantle. *Journal of Geophysical Research*, 76(8493-8515), 1971.

G. K. Batchelor. *An Introduction to Fluid Dynamics.* Cambridge University Press, Cambridge, UK, 1967.

Michael Bevis. Seismic slip and down-dip strain rates in Wadati-Benioff Zones. *Science*, 240:1317–1319, 1988.

Magali I. Billen and Michael Gurnis. A low viscosity wedge in subduction zones. *Earth and Planetary Science Letters*, in press.

J. H. Bodine and A. B. Watts. On lithospheric flexure seaward of the bonin and mariana trenches. *Earth and Planetary Science Letters*, 43:132–148, 1979.

Michael R. Brudzinski and Wang-Ping Chen. Variations in P wave speeds and outboard earthquakes: Evidence for a petrologic anomaly in the mantle transition zone. *Journal of Geophysical Research*, 105:21661–21682, 2000.

Susanne J. H. Buiter, Rob Govers, and M. J. R. Wortel. A modeling study of vertical surface displacements at convergent plate margins. *Geophysical Journal International*, submitted.

Clement G. Chase. Extension behind island arcs and motions relative to hot spots. *Journal of Geophysical Research*, 83:5385–5387, 1978.

Wang-Ping Chen and Michael R. Brudzinski. Evidence for a large-scale remnant of subducted lithosphere beneath Fiji. *Science*, 292:2475–2479, 2001.

Clinton P. Conrad and Bradford H. Hager. Effects of plate bending and fault strength at subduction zones on plate dynamics. *Journal of Geophysical Research*, 104: 17551–17571, 1999.

J. H. Davies and D. J. Stevenson. Physical model of source region of subduction zone volcanics. *Journal of Geophysical Research*, 97:2037–2070, 1992.

Adam M. Dziewonski and Don L. Anderson. Preliminary Reference Earth Model. *Physics of Earth and Planetary Interiors*, 25:297–356, 1981.

GEBCO. General bathymetric chart of the oceans, British Oceanographic Data Centre. Computer file, February 1997.

B. H. Hager and M. A. Richards. Long-wavelength variations in Earth's geoid: physical models and dynamical implications. *Phil. Trans. R. So. Lond. A*, 328:309–327, 1989.

Bradford H. Hager. Subducted slabs and the geoid: constraints on mantle rheology and flow. *Journal of Geophysical Research*, 89(B7):6003–6015, July 1984.

Bradford H. Hager and Robert W. Clayton. *Constraints on the structure of mantle convection using seismic observations, flow models, and the geoid*, chapter 9, pages 657–764. Gordon and Brack Science Publishers, 1989.

Bradford H. Hager, Robert W. Clayton, Mark A. Richrads, Robert P. Comer, and Adam M. Dziewonski. Lower mantle heterogeneity, dynamic topography and the geoid. *Nature*, 313:541–545, 1985.

Bradford H. Hager and Richard J. O'Connell. A simple global model of plate dynamics and mantle convection. *Journal of Geophysical Research*, 86:4843–4867, 1981.

Akira Hasegawa, Dapeng Zhao, Shuichiro Hori, Akira Yamamoto, and Shigeki Horiuchi. Deep structure of the Northeastern Japan Arc and its relationship to seismic and volcanic activity. *Nature*, 352:683–689, August 1991.

G. Hirth and D. L. Kohlstedt. Water in the oceanic upper mantle: implications for rheology, melt extraction and the evolution of the lithosphere. *Earth and Planetary Science Letters*, 144:93–108, 1996.

William E. Holt. Flow fields within the Tonga slab determined from the moment tensors of deep earthquakes. *Geophysical Research Letters*, 22(8):989–992, April 1995.

Gregory A. Houseman and David Gubbins. Deformation of subducted oceanic lithosphere. *Geophysical Journal International*, 131:535–551, 1997.

T. J. R. Hughes. *The Finite Element Method*. Prentice-Hall, Englewood Cliffs, NJ, 1987.

Bryan Isacks and Peter Molnar. Distibution of stress in descending lithosphere from a global survey of focal-mechanism solutions of mantle earthquakes. *Reviews of Geophysics and Space Physics*, 9:103, 1971.

M. J. Jacoby and H. Schmeling. On the effects of the lithosphere on mantle convection and evolution. *Physics of Earth and Planetary Interiors*, 29:305–319, 1982.

S. Karato. Mapping water content in the upper mantle. In J. Eiler, editor, *Subduction Factory, AGU Monograph*, Washington D. C., in press. American Geophysical Union.

S. Karato and H. Jung. Water, partial melting and the origin of the seismic low velocity and high attenuation zone in the upper mantle. *Earth and Planetary Science Letters*, 157:193–207, 1998.

S. Karato and H. Jung. Effects of pressure on high-temperature dislocation creep in olivine. *Philosophical Magazine Annals*, submitted.

P. B. Kelemen, G. Hirth, N. Shimizu, M. Spiegelman, and H. J. B. Dick. A review of melt migration processes in the adiabatically upwelling mantle beneath spreading ridges. *Philosophical Transactions Royal Society London Annals*, 355:283–318, 1997.

Scott D. King. Models of mantle viscosity. In *Mineral Physics and Crystallography, AGU Reference Shelf*, pages 227–236. American Geophysical Union, 1995.

Dorothy M. Koch and Neil M. Ribe. The effect of lateral viscosity variations on surface observables. *Geophysical Research Letters*, 16:535–538, 1989.

D. L. Kohlstedt, Brian Evans, and S. J. Mackwell. Strength of the lithosphere: constraints imposed by laboratory experiments. *Journal of Geophysical Research*, 100:17587–17602, 1995.

D. L. Kohlstedt, H. Keppler, and D. C. Rubie. Solubility of water in a, b, and g phases of $(Mg,Fe)_2SiO_4$. *Contribution to Mineralogy and Petrology*, 123:345–357, 1996.

V. V. Kostrov. Seismic moment and energy of earthquakes, and seismic flow of rock. *Earth Physics*, 1:13–20, 1974.

L. W. Kroenke. *Cenozoic Tectonic Development of the Southwest Pacific*. U.N. ESCAP CCOP/SOPAC Tech. Bull. 6, New Zealand, 1984.

Kurt Lambeck. *Geophysical Geodesy: the slow deformations of the Earth*. Oxford University Press, 1988.

Marianna Lee and Robert Powell, editors. *Initial Reports of the Deep Sea Drilling Program*, chapter 1, pages 4–45. U. S. Gov. Print. Off., Washington, D. C., 1982.

F. G. Lemoine, S. C. Kenyon, J. K. Factor, R. G. Trimmer, N. K. Pavlis, and et al. The Development of the Joint NASA GSFC and NIMA Geopotential Model EGM96. Technical report, NASA Goddard Space Flight Center, Greenbelt, Maryland, 1998.

David C. McAdoo. On the compensation of geoid anomalies due to subducting slabs. *Journal of Geophysical Research*, 87:8684–8692, 1982.

Dan P. McKenzie. Speculations on the consequences and causes of plate motions. *Geophysical Journal of the Royal Astornomical Society*, 18:1–32, 1969.

S. Mei. *The effect of water on the plastic deformation on olivine and olivine-basalt aggregates*. PhD thesis, University of Minnesota, 1999.

H. J. Melosh. Dynamic support of the outer rise. *Geophysical Research Letters*, 5: 321–324, 1978.

Louis Moresi and Michael Gurnis. Constraints on the lateral strength of slabs from three-dimensional dynamic flow models. *Earth and Planetary Science Letters*, 138: 15–28, 1996.

Louis Moresi, Shijie Zhong, and Michael Gurnis. The accuracy of finite element solutions of Stokes' flow with strongly varying viscosity. *Earth and Planetary Science Letters*, 97:83–94, 1996.

Louis N. Moresi and V. S. Solomatov. Numerical investigations of two-dimensional convection with extremely large viscosity variations. *Physics of Fluids*, 9:2142–2162, 1995.

J. D. Morris, W. P. Leeman, and F. Tera. The subducted component in island arc lavas: constraints from Be isotopes and B-Be systematics. *Nature*, 344:31–36, 1990.

R. D. Müller, W. R. Roest, J. Y. Royer, L. M. Gahagan, and J. G. Sclater. Digital isochrons of the world's ocean floor. *Journal of Geophysical Research*, 102:3211–3214, 1997.

R. D. Müller, J. Y. Royer, and L. A. Lawver. Revised plate motions relative to the hotspots from combined Atlantic and Indian hotspot tracks. *Geology*, 21:275–278, 1993.

Sarah Nothard, John Haines, James Jackson, and Bill Holt. Distributed deformation in the subducting lithosphere at Tonga. *Geophysical Journal International*, 127: 328–338, 1996.

Yujiro Ogawa, Kazuo Kobayashi, Hiroshi Hotta, and Kantaro Fujioka. Tension cracks on the oceanward slopes of the northern Japan and Mariana Trenches. *Marine Geology*, 141:111–123, 1997.

Henry N. Pollack. Spherical harmonic representation of the gravitational potential of a point mass, a spherical cap and a spherical rectangle. *Journal of Geophysical Research*, 78:1760–1768, 1973.

R. W. Raitt, R. L. Fisher, and R. G. Mason. Tonga Trench. In *Geological Society of America, Special Paper, Crust of the Earth*, volume 62, pages 237–254. Waverly Press, Baltimore, Maryland, 1955.

M. A. Ravine and J. Phipps Morgan. Geoid effect of lateral viscosity variations near the top of the mantle: a 2-d model. *Earth and Planetary Science Letters*, 119: 617–625, 1993.

Y. Ricard, C. Froidevaux, and L. Fleitout. Global plate motion and the geoid: a physical model. *Geophysical Journal*, 93:477–484, 1988.

Mark A. Richards and Bradford H. Hager. Geoid anomalies in a dynamic earth. *Journal of Geophysical Research*, 89:5987–6002, 1984.

Mark A. Richards and Bradford H. Hager. Effects of lateral viscosity variations on long-wavelength geoid anomalies an topography. *Journal of Geophysical Research*, 94:10299–10313, 1989.

A. E. Ringwood. Phase transformations and differentiation in subducted lithosphere: implications for mantle dynamics, basalt petrogenesis, and crustal evolution. *Journal of Geology*, 90:611–643, 1982.

E. Roth, D. Wiens, and D. Zhao. An empirical relationship between seismic attenuation and velocity anomalies in the upper mantle. *Geophysical Research Letters*, 27:601–604, 2000.

Erich G. Roth, Douglas A. Wiens, Leroy M. Dorman, John Hildebrand, and Sphar C. Webb. Seismic attenuation tomography of the Tonga-Fiji region using phase pair methods. *Journal of Geophysical Research*, 104:4795–4809, 1999.

Robertao Sabadini, Carlo Giunchi, Paolo Gasperini, and Enzo Boschi. Plate motion and dragging of the upper mantle: lateral variations of lithospheric thickness and their implications for intraplate deformation. *Geophysical Research Letters*, 19: 749–752, 1992.

C. H. Scholz and J. Campos. On the mechanism of seismic coupling and back arc spreading at subduction zones. *Journal of Geophysical Research*, 100:22103–22115, 1995.

Tetsuzo Seno and Yoshiko Yamanaka. Arc stresses determined by slabs: Implications for mechanisms of back-arc spreading. *Geophysical Research Letters*, 25(27):3227–3230, September 1998.

Mark Simons. *Localization of Gravity ond Topography: Constraints on the Tectonics and Mantle Dynamics of Earth and Venus.* PhD thesis, Massachusetts Insititute of Technology, Boston, MA, 1996.

Norman H. Sleep. Stress and flow beneath island arcs. *Geophysical Journal International*, 42:827–857, 1975.

Seth Stein and Carol Stein. Thermo-mechanical evolution of oceanic lithosphere: implications for the subduction process and deep earthquakes. In *Subduction Top to Bottom*, volume 96 of *Geophysical Monograph*, pages 1–17. American Geophysical Union, 1996.

Edward Stolper and Sally Newman. The role of water in the pertogenesis of Mariana trough magmas. *Earth and Planetary Science Letters*, 121:293–325, 1994.

Y. Tatsumi, M. Sakayuma, H. Fukuyama, and I. Kushiro. Generation of arc basalt magmas and thermal structure of the mantle wedge in subduction zones. *Journal of Geophysical Research*, 88:5815–5825, 1983.

Catherine Thoraval and Mark A. Richards. The geoid constraint in global geodynamics: viscosity structure, mantle heterogeneity models and boundary conditions. *Geophysical Journal International*, 131:1–8, 1997.

K. E. Torrance and D. L. Turcotte. Thermal convection with large viscosity variations. *Journal of Fluid Mechanics*, 47:113–125, 1971.

D. L. Turcotte, D. C. McAdoo, and J. G. Caldwell. An elastic-prefectly plastic analysis of the bending of the lithosphere at a trench. *Tectonophysics*, 47:193–208, 1978.

Rob van der Hilst. Complex morphology of subducted lithosphere in the mantle beneath the Tonga Trench. *Nature*, 374:154–157, March 1995.

M. S. Vassiliou, B. H. Hager, and A. Raefsky. The distribution of earthquakes with depth and stress in subducting slabs. *Journal of Geodynamics*, 1:11–28, 1984.

C. Vigny, Y. Ricard, and C. Froidevaux. The driving mechanism of plate tectonics. *Tectonophysics*, 187:345–360, 1991.

Lianxing Wen and Don L. Anderson. Present-day plate motion constraint on mantle rheology and convection. *Journal of Geophysical Research*, 102:24639–24653, 1997.

Shuxia Zhang and Ulrich Christensen. Some effects of lateral viscosity variations on geoid and surface velocities induced by density anomalies in the mantle. *Geophysical Journal International*, 114:531–546, 1993.

D. Zhao, A. Hasegawa, and S. Horiuchi. Tomographic imaging of P and S wave velocity structure beneath Northeastern Japan. *Journal of Geophysical Research*, 97:19909–19928, 1992.

Dapeng Zhao, Yingbiao Xu, Douglas A. Wiens, LeRoy Dorman, John Hildebrand, and Spahr Webb. Depth extent of the Lau Back-arc Spreading Center and its relation to subduction processes. *Science*, 278:254–257, October 1997.

S. Zhong, M. T. Zuber, L. Moresi, and M. Gurnis. Role of temperature-dependent viscosity and surface plates in spherical shell models of mantle convection. *Journal of Geophysical Research*, 105:11063–11082, 2000.

Shijie Zhong. Analytic solutions for Stokes' flow with lateral variations in viscosity. *Geophysical Journal International*, 124:18–28, 1996.

Shijie Zhong and Geoffrey F. Davies. Effects of plate and slab viscosities on the geoid. *Earth and Planetary Science Letters*, 170:487–496, 1999.

Shijie Zhong and Michael Gurnis. Viscous flow model of a subduction zone with a faulted lithosphere: long and short wavelength topography, gravity and geoid. *Geophysical Research Letters*, 19(18):1891–1894, September 1992.

Shijie Zhong and Michael Gurnis. Controls on trench topography from dynamic models of subducted slabs. *Journal of Geophysical Research*, 99(B8):15683–15695, August 1994.

Shijie Zhong and Michael Gurnis. Interaction of weak faults and Non-Newtonian rheology produces plate tectonics in a 3-D model of mantle flow. *Nature*, 383: 245–247, 1996.

Shijie Zhong, Michael Gurnis, and Gregory Hulbert. Accurate determination of surface normal stress in viscous flow from a consistent boundary flux method. *Physics of Earth and Planetary Interiors*, 78:1–8, 1993.

Shijie Zhong, Michael Gurnis, and Louis Moresi. Free-surface formulation of mantle convection - I. basic theory and application to plumes. *Geophysical Journal International*, 127:708–718, 1996.

Shijie Zhong, Michael Gurnis, and Louis Moresi. Role of faults, nonlinear rheology, and viscosity structure in generating plates from instantaneous mantle flow models. *Journal of Geophysical Research*, 103(B7):15255–15268, July 1998.